Highlights

Theoretical Modeling of a Bottom-Raised Oscillating Surge Wave Energy Converter Structural Loading and Power Performance

Nhu Nguyen, Jacob Davis, Nathan Tom, Krish Thiagarajan

- Closed-form equations are developed for an OSWEC's pitch-pitch and surgepitch added mass, radiation damping, and excitation forces/torques, which can be used to determine the system's response amplitude operator (RAO) and foundation loads.
- The proposed model is benchmarked against numerical simulations using WAMIT and WEC-Sim; excellent agreement is found.
- The flat plate assumption, inherent to the theoretical model, was examined through comparison with numerical solutions over a range of plate thickness.
- A case study demonstrates the ability of the analytical model to quickly (less than one second per frequency) sweep over a domain of OSWEC dimensions, illustrating the model's utility in the early phases of design.

Theoretical Modeling of a Bottom-Raised Oscillating Surge Wave Energy Converter Structural Loadings and Power Performances

Nhu Nguyen^a, Jacob Davis^b, Nathan Tom^c, Krish Thiagarajan^d

^aSandia National Laboratories, Albuquerque, NM 87123, USA.

^b Department of Civil and Environmental Engineering, University of Washington, Seattle, WA 98195. USA.

^cNational Renewable Energy Laboratory (NREL), Golden, CO 80401, USA
^d Department of Mechanical and Industrial Engineering, University of Massachusetts Amherst,
Amherst MA 01003, USA.

Abstract

This study presents theoretical formulations to evaluate the fundamental parameters and performance characteristics of a bottom-raised oscillating surge wave energy converter (OSWEC) device. Employing a flat plate assumption and potential flow formulation in elliptical coordinates, closed-form equations for the added mass, radiation damping, and excitation forces/torques in the relevant pitch-pitch and surge-pitch directions of motion are developed and used to calculate the system's response amplitude operator and the forces and moments acting on the foundation. The model is benchmarked against numerical simulations using WAMIT and WEC-Sim, showcasing excellent agreement. The sensitivity of plate thickness on the analytical hydrodynamic solutions is investigated over several thickness-to-width ratios ranging from 1:80 to 1:10. The results show that as the thickness of the benchmark OSWEC increases the deviation of the analytical hydrodynamic coefficients from the numerical solutions grows from 3% to 25%. Differences in the excitation forces and torques, however, are contained within 12%. While the flat plate assumption is a limitation of the proposed analytical model, the error is within a reasonable margin for use in the design space exploration phase before a higher-fidelity (and thus more computationally expensive) model is employed. A parametric study demonstrates the ability of the analytical model

to quickly sweep over a domain of OSWEC dimensions, illustrating the analytical model's utility in the early phases of design.

Keywords: theoretical model, analytical, hydrodynamic coefficients, OSWEC, WEC-Sim, WAMIT, wave energy, design optimization, structural loads, and power production.

1. Introduction

In light of detrimental environmental issues, including acid rain and global warming, the transition from traditional energy sources, such as petroleum and coal, is urgent and necessary. In addition to wind and solar energy, wave energy converters (WECs) have long been considered a competitive candidate in capturing and converting energy from surface waves into usable electricity (Ross, 1995). With an estimated 30,000 trillion watt-hours per year in untapped wave energy available worldwide (Folley and Whittaker, 2009), research interests in this area have been growing significantly in recent years. Real-world projects have been proposed for both near-shore and offshore applications (Malali and Marchand, 2020). WEC systems have also been examined at the utility scale and as an auxiliary power supply to other structures in remote locations such as marine aquaculture and remotely operated underwater vehicles (Foteinis and Tsoutsos, 2017). Depending on the application, as well as the environmental conditions at the site, a wide variety of working principles have been explored. Two of the most popular principles include the point absorber (a floating disk that extracts energy mostly from heave motions, e.g., Coe et al., 2019) and the oscillating wave surge converter (a bottom-hinged, buoyant flap that harvests energy from the orbital motions of waves, e.g., Yu et al., 2014 and Choiniere et al., 2022).

Despite widespread effort, the development of wave energy extraction remains mostly confined to the research and development stage, with only a few systems having been installed in real site conditions (Malali and Marchand, 2020). These include the Power Buoy by Ocean Power Technologies Inc. deployed in Hawaii (Ocean Power Technologies, 2020), the Pelamis at Agučadoura Wave Park, Portugal (Drew et al., 2009), the Oyster at Orkney, Scotland (Cameron et al., 2010), and the WaveRoller at Peniche, Portugal (Kasanen, 2015). To the authors' knowledge, no commercial wave energy converter has been installed. Presently, the wave energy

development community has identified high structural costs as the primary driver of a WEC prototype's levelized cost of energy (LCOE), which could ultimately determine the economic viability as well as commercial realization of such a device (Jenne et al., 2015).

Reducing the cost of wave energy converter technology is essential for its advancement. Optimizing structural design was identified as one of the four most promising pathways in the development of WECs, as it can account for up to a 31% reduction in average lifetime costs (Ochs and Bull, 2013). The work presented here is part of a joint project between the Ocean Resources and Renewable Energy group at the University of Massachusetts Amherst and the National Renewable Energy Laboratory, which aims to optimize the structural cost and power production of a bottom-raised oscillating surge wave energy converter (OSWEC). One of the important advantages of a bottom-raised OSWEC (compared to bottom-fixed) is that the system can be placed further offshore without having to uniformly increase the device dimensions, which can lessen the associated costs of the support structures in the vertical direction. For this project, the ability to predict these parameters quickly and accurately is essential in achieving the objectives.

Various methods, including analytical, semi-numerical, and numerical models, were explored to assess the structural loads on the OSWEC and its foundation in response to a range of wave conditions. Among these approaches, theoretical models prevailed due to their simple setup and quick computation time. This approach, however, is limited to simple geometries (e.g., circular or elliptical cylinders, Zheng and Zhang, 2016; Chatjigeorgiou and Katsardi, 2018). In the WEC application, one of the notable studies employing this approach is from Michele et al. (2016). The authors solve the radiation and scattering potentials for bottom-fixed OSWEC systems using angular and radial Mathieu functions. The potential flow problem is transformed into the elliptical coordinates, in which the thickness of the device can be set equal to zero, allowing the problem to

be solved with a closed-form solution. The hydrodynamic coefficients predicted by their model (added mass and radiation damping) compare well with experimental data.

For semi-numerical techniques, Renzi and Dias's series of papers have proposed using Green's integral theorem along with a hyper-singular integral in the potential flow equation to predict the hydrodynamics of a single OSWEC with negligible thickness (Renzi and Dias, 2012, 2013a, 2013b). The method has been applied to study OSWEC performance in both the open ocean and in a channel. Michele et al. (2015) later extended the integral approach to study the motions of an array of devices with finite thickness. Employing a different approach, Noad and Porter (2015) introduced Fourier transforms and Galerkin expansion methods to study the behaviors of both surface-piercing and fully submerged OSWECs. The results from these models compare favorably with experimental data. Semi-numerical techniques, however, have not been widely adopted by the community due to the unavailability of ready-to-use tools and/or the requirement for extensive numerical programming. The computational time is typically 1 to 2 orders of magnitude larger than that of analytical solutions.

The third approach is numerical methods, which are generally not limited to certain geometric features and are thus employed more widely to research WEC system motions. Within this approach, the boundary element method (BEM) is popular due to its relatively quick computational speed compared to other methods such as computational fluid dynamics (CFD). Many studies have employed this technique to investigate OSWEC performance (e.g., van Rij et al., 2019; Schmitt and Elsaesser, 2015; Trueworthy and DuPont, 2020). Notable BEM software employed in WEC design includes Capytaine, Nemoh, and WAMIT. While the first two programs are freely distributed, open-source, and written in Python and FORTRAN, respectively, the latter is commercial and requires a license to use. The common objective of these programs is to

numerically obtain the velocity potential solutions of the potential flow boundary-value problem in the frequency domain. They differ in their approach, however, with some utilizing Green's theorem to directly solve for the velocity potential and others employing the source formulation, in which the velocity potential is expressed as a distribution of source functions. Both methods involve finding the solutions to the integral of the Green's function and/or its derivatives numerically. To expand the use of the hydrodynamic solutions beyond frequency analysis, WEC-Sim (Wave Energy Converter SIMulator) is often employed to simulate the WEC systems in the time domain, where they can be coupled with controls, power take-off systems, and other external bodies and forces (Yu et al., 2020). Similar to the semi-numerical technique, numerical modeling also requires significant user and computational efforts, which can inhibit the fine-scale parametrization of objective dimensions.

The initial sizing of a wave energy converter is an iterative process that relies on knowledge of the relevant hydrodynamic coefficients for a wide range of geometric parameters. For this reason, analytical models are often the most effective and least time-consuming approach. In the current study, a theoretical formulation is developed to rapidly evaluate the fundamental parameters of a bottom-raised OSWEC based on its response amplitude operator (RAO), foundation load, and hydrodynamic coefficients. While the first two variables are derived from the equations of motion, the hydrodynamic coefficients (the added mass and radiation), which are the highlight of this work, are formulated by extending the work introduced in Michele et al. (2016). In addition to the pitch-pitch hydrodynamic coefficients, the current study includes derivations for the surge-pitch added mass and radiation damping, which are needed for a complete calculation of the foundational loads and power estimates. Note that the two sets of hydrodynamic coefficients are developed in this study: one is for the OSWEC pitching at the hinge and one is for the OSWEC

pitching at the center of gravity. The former set is used directly in the analytical formulas to calculate structural loading. The latter set is useful for compatibility with WEC-Sim, which requires the input hydrodynamic coefficients used in rotational modes to be strictly defined around the center of gravity (as was done in WAMIT for comparison).

The OSWEC in this study is assumed to be a simple flat plate with negligible thickness connected to a fixed foundation (Fig. 1). The proposed analytical model is benchmarked against numerical simulations including 1) a comparison of hydrodynamic coefficients with output from WAMIT, and 2) a comparison of the foundation force reaction and RAO with output from WEC-Sim. For the remainder of the paper, Section 2 presents the theoretical formulations for the hydrodynamic coefficients in pitch-pitch and surge-pitch directions, the RAO, and the structural loads. Section 3 describes the validation test cases and comparisons with WAMIT and WEC-Sim solutions. Section 4 presents discussion on the model's sensitivity to OSWEC thickness and the limitation of the flat plate assumption. The section also demonstrates the usefulness of the proposed model through a parametric study over a range of geometric dimensions using capture width ratio and structural loading as objectives. Section 5 concludes and summarizes key points from the study.

2. Theoretical Model

2.1. Governing Dynamics

This section presents a set of formulations to predict the foundational loads and system responses of a bottom-raised OSWEC due to wave excitation. The OSWEC has the simple geometry with negligible thickness shown in Fig. 1. Since the OSWEC system is constrained to pitch motion only, the equations of motions are first established employing the sum of moments at the hinge. Using frequency domain analysis, characteristics of foundation loads and RAOs are then derived as functions of incoming wave properties, hydrodynamic and hydrostatic coefficients, and any external forces such as those from attached springs and the power take-off (PTO) system. The analytical model does not consider body-to-body radiation interaction effects between the flap and the foundation.

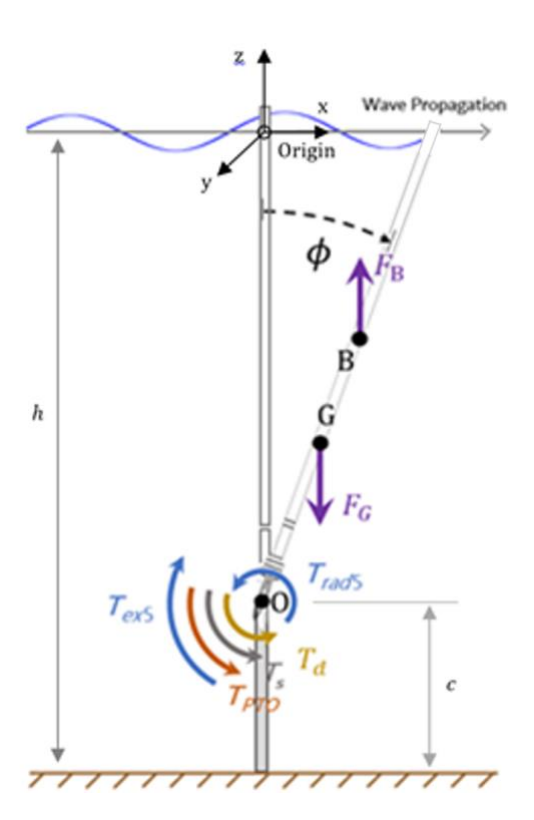


Figure 1 – Bottom-raised OSWEC geometry, showing the foundation of height c in water of depth h. The flap motion is denoted as $\phi(t)$. The flap is assumed to be a thin plate of negligible thickness.

2.1.1. Force and Torque Balances

The OSWEC is constrained to move in the pitch direction. The general one degree of freedom equation of motion is derived from the balance of torques as

$$I_{55}\ddot{\phi} = T_{ex5} + T_{rad5} + T_G + T_B + T_{PTO} + T_S + T_d \tag{1}$$

where I_{55} is the pitch moment of inertia about the hinge, and $\ddot{\phi}$ is the second time derivative of the pitch displacement ϕ , or the pitch angular acceleration. T_G and T_B are gravity and buoyancy torques, which produce counteracting moments about the hinge O (Fig. 1). T_{ex5} and T_{rad5} denote the excitation and radiation torques in the pitch direction of motion. Additional torques, resulting from the PTO (T_{PTO}), external springs (T_S), and viscous sources (T_d), also contribute moments about the hinge.

2.1.2. Equation of Motion in the Frequency Domain

In the case of regular, monochromatic waves, the incident wave elevation is described by linear wave theory as

$$\eta(x,t) = \Re\{ae^{i(\omega t - kx)}\}\tag{2}$$

where a is the wave amplitude, or half the wave height H, i is the imaginary unit, ω is the angular frequency, and k is the wavenumber. Setting the origin along the mean position of the flap (Fig. 1), the harmonic response of the OSWEC in pitch motion is then described as

$$\phi(t) = \Re{\{\tilde{\phi}e^{i\omega t}\}} \tag{3}$$

$$\dot{\phi}(t) = \Re\{i\omega\tilde{\phi}e^{i\omega t}\}\tag{4}$$

$$\ddot{\phi}(t) = \Re\{-i\omega^2 \tilde{\phi} e^{i\omega t}\} \tag{5}$$

where $\tilde{\phi}$ is the complex pitch amplitude composed of the pitch magnitude $|\phi|$ and a phase $\angle \phi$

$$\tilde{\phi} = |\phi|e^{i\angle\phi} \tag{6}$$

The torques on the right-hand side of Equation (1) can now be expressed as functions of frequency as following (Techet, 2005; Gomes et al., 2015):

$$T_{ex5}(\omega) = \Re\{aX_5(\omega)e^{i\omega t}\}\tag{7}$$

$$T_{rad5}(\omega) = \Re\{-\omega^2 A_{55}(\omega)\tilde{\phi}e^{i\omega t} + i\omega B_{55}(\omega)\tilde{\phi}e^{i\omega t}\}$$
 (8)

where X_5 is the frequency-dependent complex pitch excitation torque per unit wave amplitude, again composed of an ordinary amplitude $|X_5|$ and phase $\angle X_5$. The radiation torque, on the other hand, is represented as the linear sum of the added mass and radiation damping contributions, which are in phase with the OSWEC angular acceleration and velocity, respectively. Here, A_{55} is the frequency-dependent pitch added moment of inertia and B_{55} is the pitch radiation damping coefficient. The torque contributions due to gravity and buoyancy are (Gomes et al., 2015, Choiniere et al. 2019)

$$T_G = -mgr_q \sin(\phi(t)) \tag{9}$$

$$T_B = \rho g V r_b \sin(\phi(t)) \tag{10}$$

where m is the OSWEC body mass, V is its displaced volume, g is the acceleration of gravity, ρ is the fluid density, $r_g \equiv \overline{OG}$ is the distance measured from the hinge axis to the center of gravity, and $r_b \equiv \overline{OB}$ is the distance from the hinge axis to the center of buoyancy. These two contributions are combined to obtain a net restoring torque

$$T_{hs} = T_G + T_B = (\rho V r_b - m r_a) g \sin(\phi(t))$$
(11)

with

$$C_{55} = \rho V r_b - m r_g \tag{12}$$

The coefficients are grouped into a hydrostatic restoring coefficient, denoted C_{55} , and the *sine* term is linearized under the assumption that, for small pitch displacements, $\sin(\phi(t)) \approx \phi(t)$:

$$T'_{hs}(\omega) = C_{55}\phi(t) = \Re\{C_{55}\tilde{\phi}e^{i\omega t}\}\tag{13}$$

The power take-off also applies a torque on the OSWEC as it extracts energy. Depending on the type of PTO system used, the applied torque can have components that are in phase with both velocity and position (Kelly et al., 2017):

$$T_{PTO}(\omega) = \Re\{i\omega B_{PTO}\tilde{\phi}e^{i\omega t} + C_{PTO}\tilde{\phi}e^{i\omega t}\}$$
(14)

Here, B_{PTO} and C_{PTO} are the PTO damping and restoring coefficients, respectively. Depending on the capabilities of the PTO and the control scheme, these coefficients can be time-varying or constant.

The remaining two torque contributions, which account for externally attached springs and viscous damping sources, are described as

$$T_s(\omega) = \Re\{C_{ext}\tilde{\phi}e^{i\omega t}\}\tag{15}$$

$$T_d(\omega) = \Re\{i\omega B_v \tilde{\phi} e^{i\omega t}\}$$
 (16)

where C_{ext} is the net restoring coefficient of any externally attached springs and B_{v} is the net damping coefficient, composed of any viscous sources that can be approximated as linearly proportional to the pitch angular velocity (Nguyen et al., 2023).

The expressions in Equations (7)–(16) are substituted into the general equation of motion (Equation (1)), and rearranged to obtain the frequency domain equation of motion as

$$\Re\{[-\omega^{2}(I_{55} + A_{55}(\omega)) + i\omega(B_{55}(\omega) + B_{PTO} + B_{v}) + (C_{55} + C_{PTO} + C_{ext})]\tilde{\phi}e^{i\omega t}\}$$

$$= \Re\{aX_{5}(\omega)e^{i\omega t}\}$$
(17)

Dropping the time-dependent sine terms, the equation of motion in its final form is:

$$\tilde{\phi} \left[-\omega^2 \left(I_{55} + A_{55}(\omega) \right) + i\omega (B_{55}(\omega) + B_{PTO} + B_{v}) + (C_{55} + C_{PTO} + C_{ext}) \right] = a X_5(\omega) \quad (18)$$

2.2.Structural Loadings

2.2.1. Hinge Reaction Forces

Neglecting centrifugal forces, the surge and heave reaction forces, F_{r1} and F_{r3} , at the hinge (point O in Fig. 2) of a fore-aft symmetrical OSWEC can be described in the frequency domain as (Kurniawan and Moan, 2012)

$$F_{r1}(\omega) = \left(-\omega^2 A_{15}(\omega) + i\omega B_{15}(\omega)\right)\tilde{\phi} - aX_1(\omega) \tag{19}$$

$$F_{r3}(\omega) = -(\rho V - m) - aX_3(\omega) \tag{20}$$

where A_{15} and B_{15} are the surge-pitch added mass and surge-pitch radiation damping coefficients, respectively. X_1 and X_3 denote the complex surge and heave excitation forces per unit wavelength. The surge reaction force is composed entirely of dynamic terms that result from the motion of the OSWEC itself and the incident wave load. The heave reaction force, on the other hand, is composed of a static contribution from the net hydrostatic forces and a time-varying wave load component. Due to the thin plate assumption, the heave reaction force is not calculated in the analytical study.

2.2.2. Foundation Shear Force and Bending Moment

Structural loads are of principal concern during the design of OSWECs. Generally, these are the result of the hinge reaction forces and power take-off torque/forces described in the previous subsections. When raised on a foundation, these dynamics induce a significant shear force and bending moment at the base of the foundation. Additionally, if the wave orbitals penetrate to the depths of the foundation, and/or if external currents are present, the hydrodynamics of the foundation itself can also contribute to this load.

Treating the foundation as its own hydrodynamic body, which is rigidly fixed to the sea bottom, the force balances and torques about point F at the base of the foundation (Fig. 2) are

$$\sum F_x = F_{fr1} + F_{r1} + F_{ex1,f} \tag{21}$$

$$\sum F_z = F_{fr3} + F_G + F_B + F_{r3} + F_{ex3,f} \tag{22}$$

$$\sum T^F = M_{fr5} + r_f F_{r1} + T_{PTO} + T_s + T_d + T_{ex5,f}$$
 (23)

where F_{fr1} , F_{fr3} , and M_{fr5} are the foundation reaction forces/torques in the surge, heave, and pitch directions; $r_f \equiv \overline{FO}$ represents the distance from the base of the foundation F to the hinge point O; and F_G and F_B are the gravitational and buoyancy forces on the foundation, separate from those of the OSWEC body force balance. $F_{ex1,f}$ and $F_{ex3,f}$ are the foundation surge excitation and heave excitation forces, respectively (distinguished from those of the OSWEC body through the use of the f subscript); $T_{ex5,f}$ is the foundation pitch excitation torque. Contrary to the OSWEC body, the foundation does not experience any radiation hydrodynamic loads, as it does not undergo any rigid body motion. There could be, however, body-body interaction effects arising from the motion of

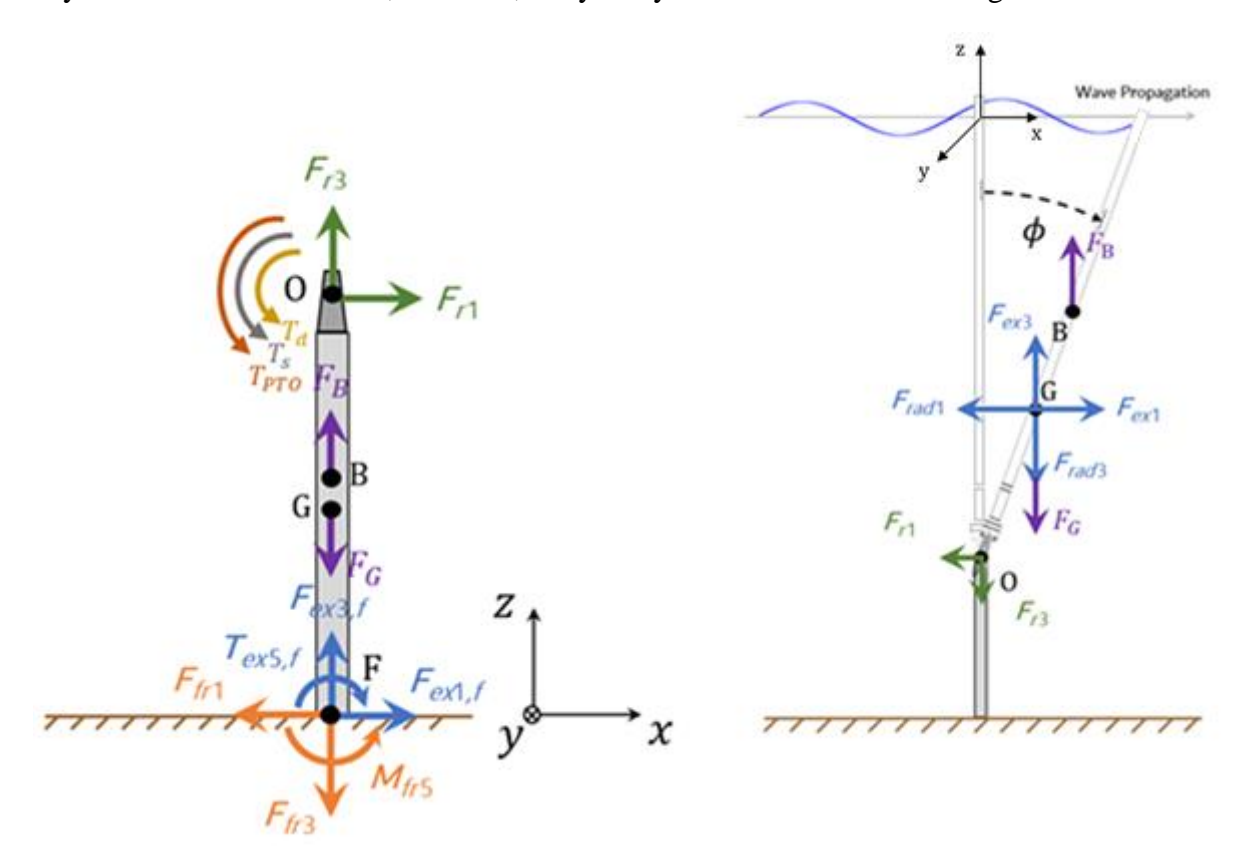


Figure 2 – (Left) Foundation force and torque balance. (Right) Forces on the flap.

the OSWEC, but as stated previously, they are not considered in the current model. F_{r1} and F_{r3} are the hinge reaction forces introduced in the OSWEC force balance (Equations (19) and (20)). These forces and torques are summarized in Fig. 2.

2.3. Performance Characterization

2.3.1. Response Amplitude Operator

The RAO represents the transfer function between the OSWEC (pitch) motion and the incident wave amplitude. For waves in the linear regime, it provides a prediction of the OSWEC pitch response for any wave period and amplitude combination. It is derived simply from the rearrangement of the frequency domain equation of motion (Equation (18)):

$$RAO \equiv \frac{\tilde{\phi}}{a} = \frac{X_5(\omega)}{\left[-\omega^2 \left(I_{55} + A_{55}(\omega)\right) + i\omega (B_{55}(\omega) + B_{PTO} + B_v) + (C_{55} + C_{PTO} + C_{ext})\right]}$$
(24)

A rotational RAO is commonly nondimensionalized by the wave number, k, of the incident wave:

$$RAO^* \equiv \frac{\tilde{\phi}}{ka} \tag{25}$$

where an asterisk has been used to distinguish the nondimensional quantity from its dimensional counterpart. The RAO will be integral to characterizing and understanding the OSWEC dynamics in subsequent sections.

2.3.2. Time-Averaged Power and Capture Width

When a PTO is simulated, the power performance of an OSWEC and its PTO system can be characterized by the commonly used nondimensional capture width (CW)

$$CW = \frac{P_T}{w P_W} \tag{26}$$

where w is the width of the OSWEC and P_T and P_W are the time-averaged power absorbed by the system and the time-averaged wave power per unit crest-width, respectively. The former is calculated in the time domain as

$$P_{T} = \frac{1}{T} \int_{t}^{t+T} P_{PTO}(t') dt'$$
 (27)

and in the special case of passive damping control, it can be obtained in the frequency domain following (Tom et al., 2017) as

$$P_{T} = \frac{1}{2} \int \frac{|X_{5}|^{2}}{B_{55}} \frac{1}{1+\varepsilon} S(\omega) d\omega$$
 (28)

 ϵ is a nondimensional coefficient (always greater than or equal to 1) employed in passive damping control model such that $B_{PTO}(\omega) = \epsilon(\omega)B_{55}(\omega)$ and

$$\epsilon(\omega) = \sqrt{1 + \left(\frac{C_{55} + C_{PTO} - \omega^2 (I_{55} + A_{55}(\omega))}{\omega B_{55}(\omega)}\right)^2}$$
(29)

This corresponds to the optimum PTO damping of the system. It is noted that this strategy implies the PTO damping can be modified on a per-wave basis, and that the PTO restoring coefficient is a constant value. The PTO damping coefficient that maximizes the instantaneous power absorbed by the PTO is related to the OSWEC body's wave radiation damping coefficient. $S(\omega)$ denotes the wave energy spectrum. In this paper, the Bretschneider Spectrum is used:

$$S(\omega) = \frac{5}{16} \frac{\omega_m^4}{\omega^5} H_{1/3}^2 \exp\left(-\frac{5}{4} \frac{\omega_m^4}{\omega^4}\right)$$
 (30)

where ω_m is the modal frequency and $H_{1/3}$ is the significant wave height. The time and spatially averaged wave power per unit crest-width is purely a function of the wave conditions and is calculated as

$$P_w = \frac{1}{2}\rho g \alpha^2 V_g \tag{31}$$

with wave group velocity

$$V_g = \frac{1}{2} \sqrt{\frac{g}{k}} \tanh kh \left(1 + \frac{2kh}{\sinh 2kh} \right) \tag{32}$$

The expressions in Equations (26–32) are evaluated for a single wave period (or frequency); thus, the capture width is typically characterized over a desired range of wave frequencies. The passive damping model and metrics will be used in subsequent sections to conduct a case study on OSWEC power output performance.

2.4. Analytical Model of Hydrodynamic Coefficients

The following work extends the analytical models originally proposed in Michele et al. (2016) for a bottom-fixed OSWEC. In the following section, the problem description and the solutions will be reformulated such that they can take into account the raised support structure. Coupling surge-pitch coefficients are also derived so that the foundational loads can be estimated (Equations (21) and (23)).

Consider a bottom-raised OSWEC with width w and height H_o hinged on a foundation of height c. The height and width dimensions of the OSWEC are significantly greater than its thickness, such that the OSWEC can be represented as a thin flap. The OSWEC pierces the surface at all pitch angles, such that no overtopping occurs (Fig. 1).

A velocity potential (or total wave potential) $\Phi(x, y, z, t)$ is sought that satisfies the Laplace equation for an inviscid, incompressible, and irrotational fluid domain:

$$\nabla^2 \Phi(x, y, z, t) = 0 \tag{33}$$

We assume that the flap undergoes regular harmonic motion with frequency ω around the y-axis (Fig. 1) as

$$\psi(t) = Re\{\Psi e^{-i\omega t}\}\tag{34}$$

Here, Ψ is the complex amplitude of rotation. The temporal component in the velocity potential can be separated out (or rewritten) as

$$\Phi(x, y, z, t) = \Re\{\widetilde{\Phi}(x, y, z)e^{i\omega t}\}\tag{35}$$

where $\widetilde{\Phi}$ is the spatial potential, which is a function of only x, y, z, and can be decomposed into a linear sum of the incident, scattered, and radiated wave potentials (Techet, 2005):

$$\widetilde{\Phi}(x, y, z) = \widetilde{\Phi}^I + \widetilde{\Phi}^S + \widetilde{\Phi}^R \tag{36}$$

with

$$\widetilde{\Phi}^{I} = -\frac{iAg}{\omega} \frac{\cosh k(h+z)}{\cosh kh} e^{-ik(x\cos\theta + y\sin\theta)}$$
(37)

Here, A is the wave amplitude, $g = 9.81 \frac{\text{m}}{\text{s}^2}$ is the gravitational constant, and i denotes the imaginary unit. θ represents the relative angle of the incident wave with respect to the x-axis, and h is the water depth. These describe the potential of the incident waves in absence of any bodies (Φ^I), the potential of the incident wave as it is modified (through diffraction) by the presence of a fixed OSWEC (Φ^S), and the potential of the waves that radiate from the moving OSWEC in the absence of any incident waves (Φ^R). It is noted that solutions of these potentials should satisfy Laplace's equation.

The governing equations are subject to the following boundary conditions (Nguyen et al., 2021):

1. Combined free surface boundary condition on z = 0:

$$g\frac{\partial \widetilde{\Phi}^{(R,S)}}{\partial z} - \omega^2 \widetilde{\Phi}^{(R,S)} = 0 \tag{38}$$

2. No-flux condition at the sea bottom, z = -h:

$$\frac{\partial \widetilde{\Phi}^{(R,S)}}{\partial z} = 0 \tag{39}$$

3. Kinematic condition (no through flow) on the flap's surfaces, $z \in [-h, 0]$, $x = \pm 0, -w/2 < y < w/2$

$$\frac{\partial \widetilde{\Phi}^R}{\partial x} = -\psi_t * (z + h - c) * H(z + h - c) = i\omega \Psi * (z + h - c)e^{-i\omega t} * H(z + h - c)$$
 (40)

$$\frac{\partial \widetilde{\Phi}^S}{\partial x} = -\frac{\partial \widetilde{\Phi}^I}{\partial x} \tag{41}$$

4.
$$\widetilde{\Phi}^S$$
 and $\widetilde{\Phi}^R$ must be bounded as $\sqrt{x^2 + y^2} \to \infty$ (42)

H is the Heaviside function to equate the OSWEC body and flow velocities over the paddle height $(H_0 = h - c)$ and to set the flow velocity to zero otherwise. A small pitch amplitude assumption has also been employed in Equation (40) such that the lateral velocity of a point on the surface of the OSWEC can be approximated by the product of the pitch velocity and the distance of the point from the hinge.

In the ordinary solution process, solutions to the diffraction, and radiation potentials are obtained in x, y, z and integrated over the body surface to derive their respective force amplitudes. The resulting forces are used to derive the added mass and radiation damping coefficients, as well as the wave excitation force and moments. Due to the complexity of the OSWEC boundary value problem, however, only semi-analytical solutions are possible in Cartesian coordinates (Renzi and Dias, 2012, 2013; Noad and Porter, 2015; Michele et al., 2016). An alternative solution process is to transform the governing equations and boundary conditions into elliptical coordinates. Following this transformation, an analytical solution can still be obtained using separation of variables. The results thus obtained can be shown to capture the physics of the more comprehensive semi-analytical and numerical methods, yet at a fraction of setup and solution time.

2.4.1. Analytical Solutions for Hydrodynamic Coefficients

The elliptical coordinate system is defined by three coordinate variables: ξ , which represents a confocal ellipse for each constant value; η , which represents a hyperbola of focal length w for

each constant angle; and z, which describes elevation (Weisstein, 2003). The Cartesian coordinates (x, y, z) are related to the elliptical coordinates (ξ, η, z) as

$$x = \frac{w}{2} \sinh \xi \sin \eta$$
 $y = \frac{w}{2} \cosh \eta \cos \xi$ $z = z$ (43)

With the focal width set to the width of the OSWEC, the body of the OSWEC is then described by the confocal ellipse at $\xi = 0$ (i.e., a flat line lying on the y-axis), $\eta \in [0,2\pi]$, and $z \in [0,-H_0]$. This configuration is best observed in the plan view (Fig. 3). With the use of Equation (43), the governing equations formed by Equations (33–36) and the four boundary conditions can be transformed into the new coordinate system and separation of variables employed to obtain solutions for $\widetilde{\Phi}^R$ and $\widetilde{\Phi}^S$.

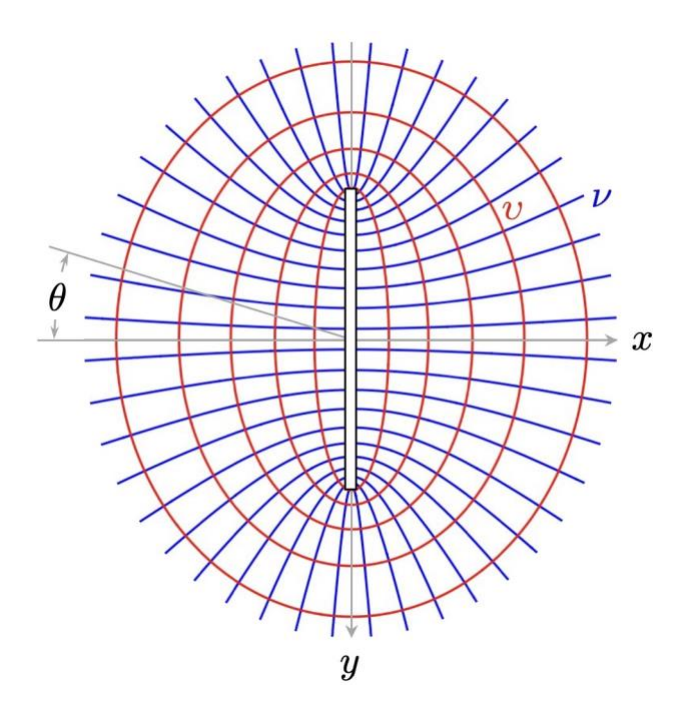


Figure 3 – OSWEC boundary value problem. Plan view in elliptical coordinates.

The expressions of $\widetilde{\Phi}^R$ and $\widetilde{\Phi}^S$ in Equation **Error! Reference source not found.** can be written using separation of variables as

$$\begin{cases} \widetilde{\Phi}^R = \varphi_n^R(x, y) Z(z) \\ \widetilde{\Phi}^S = \varphi_n^S(x, y) Z(z) \end{cases}$$
(44)

Using the conditions that both ϕ^R and ϕ^S satisfy the Laplace equation to obtain

$$Z'' - k^2 Z = 0 (45)$$

Employing boundary conditions on the water surface (Equation Error! Reference source not found.) and at the sea bottom (Equation Error! Reference source not found.), the corresponding normalized eigenfunction can be derived as (Chiang et al., 2005)

$$Z_n(z) = \frac{\sqrt{2}\cosh k_n(h+z)}{\left(h + \left(\frac{g}{\omega^2}\right)\sinh^2 k_n h\right)^{\frac{1}{2}}} , \quad n = 0,1,2,3 \dots$$
 (46)

where $k_o(n = 0) = k$ (wave number as defined previously) and k_n for $n \ge 1$ are evaluated as the root of the dispersion relations, respectively, as

$$\omega^{2} = gk \tanh(kh) , \quad n = 0$$

$$\omega^{2} = -g\kappa_{n} \tan(\kappa_{n}h) , \quad n \ge 1$$

$$\kappa_{n} = -ik_{n}$$
(47)

On the other hand, converting the Laplace equation for $\varphi^R(x,y)$ and $\varphi^S(x,y)$ to the elliptical system, the two-dimensional Helmholtz equations can be obtained as

$$\left[\frac{\partial^2}{\partial \xi^2} + \frac{\partial^2}{\partial \eta^2} + \frac{w^2 k_n^2}{8} \left(\cosh 2\xi - \cos 2\eta\right)\right] \begin{Bmatrix} \varphi^R(\xi, \eta) \\ \varphi^S(\xi, \eta) \end{Bmatrix} = 0 \tag{48}$$

The general solutions to the Helmholtz equation in these coordinates are obtained using the solutions of the angular Mathieu and Hankel-Mathieu functions. These are analogous to the use of trigonometric functions in the Cartesian system or Bessel functions in cylindrical coordinates. Applying the boundary conditions specified in Equations Error! Reference source not found.—Error! Reference source not found., the resulting solutions of the radiated and scattered potentials describing the foundation-raised OSWEC are derived as

$$\varphi_n^R(\xi,\eta) = -i\omega \Psi f_n w * \sum_{m=0}^{\infty} \frac{B_1^{(2m+1)} Ho_{2m+1}^{(1)}(0,\tau_n) se_{2m+1}(\eta,\tau_n)}{2Ho_{\xi_{2m+1}}^{(1)}(0,\tau_n)}$$
(49)

$$\varphi_n^S(\xi,\eta) = Ad_n w * \sum_{m=0}^{\infty} \frac{B_1^{(2m+1)} Ho_{2m+1}^{(1)}(0,\tau_n) se_{2m+1}(\eta,\tau_n)}{2Ho_{\xi_{2m+1}}^{(1)}(0,\tau_n)}$$
(50)

With

$$f_n = \frac{\sqrt{2}[k_n(h-c)\sinh k_n h + \cosh k_n c + \cosh k_n h]}{k_n^2 \left[h + \left(\frac{g}{\omega^2}\right)\sinh^2 k_n h\right]^{\frac{1}{2}}}, n = 0,1,2,3...$$
 (51)

$$d_n = \begin{cases} gk_o \left(h + \left(\frac{g}{\omega^2} \right) \sinh^2 k_o h \right)^{\frac{1}{2}} & n = 0\\ 0 & n \ge 1 \end{cases}$$
 (52)

$$\tau_n = \frac{1}{16}\omega^2 k_n^2 \tag{53}$$

where Ho and se are the odd Hankel-Mathieu and odd Mathieu functions of the first kind. B_1 is the first coefficient of the se function, and No is the odd radial Mathieu function of the second kind. The first subscript of $Ho_{\xi_{2m+1}}$ denotes the function is of order 2m+1 and that a derivative is to be taken with respect to the elliptical coordinate ξ . For information on Mathieu functions, refer to Gutiérrez-Vega et al. (2003).

The pitch-pitch hydrodynamic added inertia A_{55} , radiation damping B_{55} , and the wave excitation torque X_5 are also obtained (from the normal surface integral of the velocity potential derivative):

$$A_{55} = \rho w^2 \pi \sum_{n=0}^{\infty} f_n^2 Im \left\{ \sum_{m=0}^{\infty} \frac{B_1^{(2m+1)^2} N o_{2m+1}(0, \tau_n)}{4 H o_{\xi_{2m+1}^{(1)}}(0, \tau_n)} \right\}$$
 (54)

$$B_{55} = -\rho \omega w^2 f_o^2 \pi \, Re \left\{ \sum_{m=0}^{\infty} \frac{B_1^{(2m+1)^2} N o_{2m+1}(0, \tau_o)}{4 H o_{\xi_{2m+1}^{(1)}}(0, \tau_o)} \right\}$$
 (55)

$$X_5 = \rho \omega w^2 f_o d_o \pi \cos \theta \left\{ \sum_{m=0}^{\infty} \frac{B_1^{(2m+1)^2} N o_{2m+1}(0, \tau_o)}{4H o_{\xi_{2m+1}^{(1)}}(0, \tau_o)} \right\}$$
 (56)

In order to quantify the structural performance characteristics of the OSWEC, the study further develops analytical solutions for the surge wave load as following

$$A_{15} = \frac{\rho}{\omega} \sum_{n=0}^{\infty} Im \left(\iint_{S_{body}}^{\square} \phi_n^R(\xi, \eta) Z_n(z) n_1 dS \right) = \frac{\rho}{\omega} \frac{w}{2} \sum_{n=0}^{\infty} Im \left(\iint_{S_{body}}^{\square} \phi_n^R(\xi, \eta) Z_n(z) \sin \eta \, dz \, d\eta \right)$$
(57)

$$B_{15} = -\rho Re \left(\iint_{S_{body}}^{\square} \phi_o^R(\xi, \eta) Z_o(z) n_1 dS \right) = -\rho \frac{w}{2} Re \left(\iint_{S_{body}}^{\square} \phi_o^R(\xi, \eta) \sin \eta \, d\eta \, Z_o(z) dz \right) (58)$$

$$X_1 = i\omega\rho \iint_{S_{body}} \phi^S(\xi, \eta, z) n_1 dS = -i\omega\rho \frac{w}{2} \iint_{S_{body}} \phi^S(\xi, \eta) Z_o(z) \sin\eta \, dz d\eta$$
 (59)

Substituting the equations of ϕ_n^R , ϕ_n^S and $Z_n(z)$, the integral solutions can be obtained analytically to get

$$A_{15} = \rho w^2 \pi \sum_{n=0}^{\infty} f_n \lambda_n \operatorname{Im} \left\{ \sum_{m=0}^{\infty} \frac{B_1^{(2m+1)^2} N o_{2m+1}(0, \tau_n)}{4 H o_{\xi}_{2m+1}^{(1)}(0, \tau_n)} \right\}$$
(60)

$$B_{15} = \rho \omega w^2 f_o \lambda_o \pi \, Re \left\{ \sum_{m=0}^{\infty} \frac{B_1^{(2m+1)^2} N o_{2m+1}(0, \tau_o)}{4 H o_{\xi_{2m+1}^{(1)}}(0, \tau_o)} \right\}$$
(61)

$$X_{1} = \rho \omega w^{2} \lambda_{o} d_{o} \pi \cos \theta \left\{ \sum_{m=0}^{\infty} \frac{B_{1}^{(2m+1)^{2}} N o_{2m+1}(0, \tau_{o})}{4 H o_{\xi_{2m+1}^{(1)}}(0, \tau_{o})} \right\}$$
(62)

$$\lambda_n = \frac{\sqrt{2}(\sinh k_n h - \sinh k_n c)}{k_n \left(h + \frac{g}{\omega^2} \sinh^2 k_n h\right)^{\frac{1}{2}}} , n = 0,1,2,3,...$$
 (63)

Although not utilized in this model directly, the retardation function (represents free-surface memory effects), $K(i\omega)$, in frequency domain can be calculated as

$$K(i\omega) = B(\omega) + i\omega(A(\omega) - A(\infty))$$
(64)

With $A(\infty)$ is the added mass at infinite frequency and obtained by taking the limits of equations (54 and 60) corresponding to the modes of interest. The retardation function in frequency domain can be utilized to approximate the convolution term in the Cummins equation when simulating the system in time domain. For reference, comparisons of this parameter to the outputs of WAMIT are presented in Appendix A.

Using an appropriate number of orders m and terms n in the summations, the hydrodynamics can be characterized over a desired frequency range and used to obtain frequency domain results as usual. These formulas are applicable for the OSWEC placed on the sea floor or with supporting structure underneath. They can also be employed to estimate the hydrodynamic coefficients and

excitation forces/torques if the OSWEC were to pitch around its center of gravity with simple modifications in the kinematic boundary condition (Equation (40)). This results in a slight change in the f_n (distinguish by $f_{n|cq}$) equation as

$$f_{n_{|cg}} = \frac{\sqrt{2}[k_n(h-c)\sinh k_n h - 2\cosh(k_n h) + k_n(h-c)\sinh(k_n c) + 2\cosh(k_n c)]}{2k_n^2 \left[h + \left(\frac{g}{\omega^2}\right)\sinh^2 k_n h\right]^{\frac{1}{2}}}$$
(65)

The model will be benchmarked with the numerical results from WAMIT, and the results will be discussed in next section. Additionally, the analytical model is also validated by employing a second approach based on the Haskind-Hanaoka relation. The derivations and associated formulas are discussed in Appendix B along with the comparison between the two approaches.

3. Numerical Model Setup and Benchmark Studies

To substantiate the developed analytical model of a bottom-raised OSWEC, comparisons of the outputs with those from the numerical programs WAMIT and WAMIT/WEC-Sim are presented in this section. While the hydrodynamic properties, including added mass, radiation damping, and wave excitation force/torque, are benchmarked against the results from WAMIT, the response and loading on the support foundation are compared with the results from a WAMIT/WEC-Sim model. The properties of the simulated model, based on the physical model previously developed in Davis (2021), are provided in Table 1. Some deviations from the physical model are implemented to achieve a more equivalent comparison between the two models, including 1) the OSWEC thickness is scaled as 1:80 of its width to reflect the flat plate assumption used in the analytical model, 2) the support foundation is modeled as a thin rectangle with the same cross-sectional area as the OSWEC (Fig. 1), and 3) the OSWEC flap is assumed homogenous such that its mass and moment of inertia about the y-axis (Fig. 1) can be calculated as

Symbol	Property	Value	Unit
h	Water depth	1.0	m
c	Hinge to seabed	0.5	m
H_o	OSWEC height	0.5	m
W	OSWEC width	0.4	m
p	OSWEC thickness	0.005	m
M	OSWEC mass	0.85	kg
I ₅₅	Moment of inertia about the center of gravity and the hinge	0.01771,0.07084*	$kg - m^2$

²²

$$M = \rho w p H_0 = \rho V \tag{66}$$

$$I_{55_{cg}} = \frac{1}{12}M[(h-c)^2 + p^2]$$
 at the center of gravity (67)

$$I_{55_{hinge}} = I_{55_{cg}} + \frac{MH_o^2}{4}$$
 at the hinge (68)

Two benchmark cases are carried out that compare the hydrodynamic results computed at 1) the body's center of gravity and 2) the hinge location.

3.1. Numerical Model Setup and Solutions from WAMIT/WEC-Sim

Similar to the analytical solution process, where the incident, scattered, and radiated potentials are solved independently of one another and combined into a linear solution, WAMIT solves for the velocity potential and fluid pressure at each "panel" (surface mesh element) of a discretized body surface. For this project, surfaces of the geometry were discretized into panels using an external Python-based script. While hydrodynamic coefficients and excitation forces/torques for all six degrees of freedom are solved by WAMIT, only the components in surge, pitch, and heave are needed. As required by WEC-Sim, the presented hydrodynamics are computed about the center of gravity (as opposed to the hinge). Additional WAMIT runs, however, are performed about the hinge to be used for benchmarking with the analytical outputs. The WAMIT models were simulated over a frequency range of 0.1 rad/s to 20 rad/s with a step size of 0.05 rad/s.

The OSWEC and its support structure were modeled in WEC-Sim as two hydrodynamic bodies connected by a rotational PTO constraint (Fig. 4a). The rotational PTO was configured to prevent motion in all degrees of freedom except rotation about the y-axis. Due to the thin structure model, which leads to a small hydrostatic restoring force term, the OSWEC flap can easily become unstable/overturned. A small torsional restoring coefficient, $C_{PTO} = 56 \text{ kg} \cdot \text{m}^2/\text{s}^2$ is applied at the hinge (by setting the stiffness in the PTO module) to keep the OSWEC flap upright when

subjected to wave loads. Linear damping from a physical model (Davis, 2021) is also modeled with $B_{\nu}=0.316$. The foundation is rigidly connected to the seafloor by a fixed constraint. The Simulink configuration is shown in Fig. 4b. The WAMIT/WEC-Sim model is simulated with 30 cases covering a period range, T, from 0.8 s to 5.0 s (1.25 rad/s to 7.85 rad/s). The corresponding wave amplitudes are chosen such that $\frac{2a}{gT^2}=0.0001$ to keep within the linear regime. The regular convolution integral calculation class, regularCIC, was used with a convolution integral time (CITime) of 20 s and the fixed time step MATLAB solver, ODE4. A linear ramp function was applied to the incident wave forcing to prevent unwanted transients and numerical instabilities. The Multiple Condition Runs (MCR) feature was used to script the simulation process based on the wave heights, periods, ramp times, end times, and time steps provided in an external MCR case file. The wave ramp time, simulation end time, and simulation time step size were set to 20 times, 40 times, and 1/400 times the period, respectively. A summary of the WEC-Sim simulation parameters is provided in Table 2.

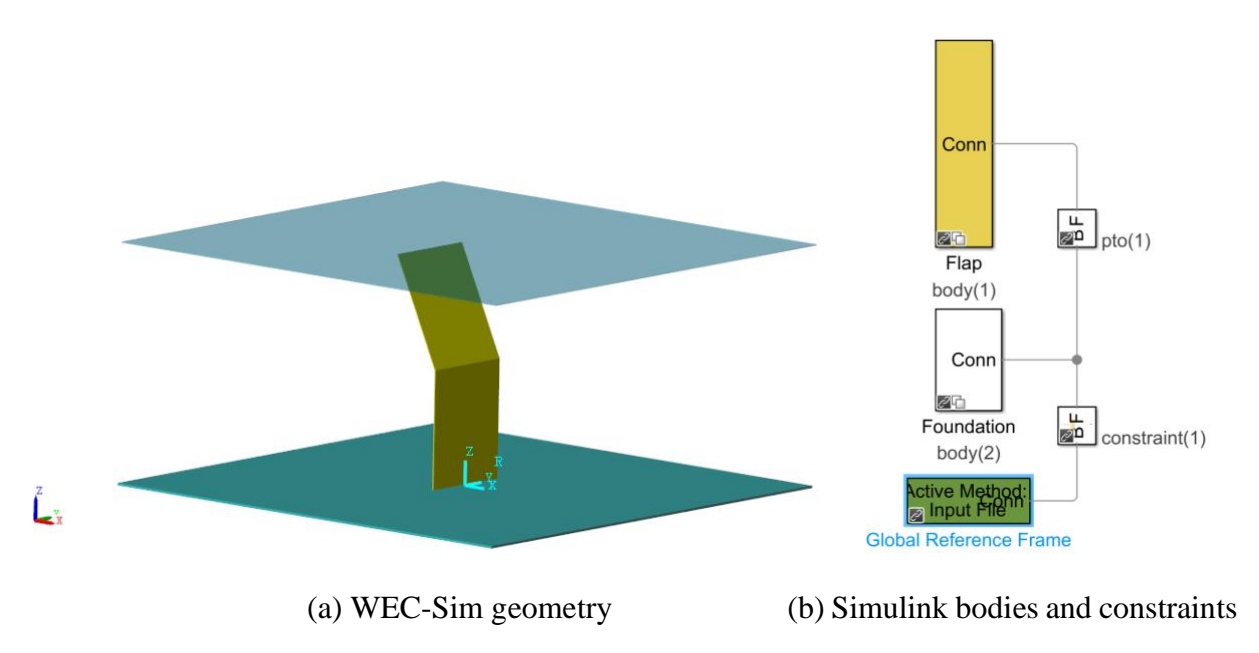


Figure 4 - WEC-Sim and Simulink setup

Table 2 - WEC-Sim simulation parameters			
Parameter	Value	Description	
Wave class	regularCIC	Regular waves with convolution integral calculation	
Solver	ODE4	Ordinary differential equation solver fixed time step	
B_{v}	0.316	Linear damping	
C_{PTO}	$56 \text{ kg} \cdot \text{m}^2 \text{s}^{-2}$	PTO torsional restoring coefficient	
dt	1/400T	Solution time step	
CITime	20 s	Convolution integral time	
rampTime	20T	Wave forcing ramp time	
endTime	40T	Simulation end time	

3.2. Hydrodynamic Coefficient Model – Comparison of Analytical Approach and WAMIT

Employing the same OSWEC specifications, analytical solutions are calculated for pitch added mass and radiation damping, surge-pitch added mass and radiation damping, surge excitation force, and pitch excitation torque over a frequency range of 0.1 rad/s to 20 rad/s with a step size of 0.05 rad/s (WAMIT output is the same). In addition, a total of 15 frequencies (n = 15) were retained in the solutions to Equations (54–63) with m = 15 to achieve convergence. The theoretical and numerical results for motions about the hinge, and about the center of gravity are compared in Figs. 5 and 6, respectively.

For motion about the hinge (Fig. 5), solutions of the hydrodynamic coefficients (A_{55} and B_{55}) show excellent comparison between the two models. The trends of the numerical model are well-captured by the analytical model, with less than 2% variations across the entire observed frequency range. Similarly, great correlations are observed for the pitch and surge excitation torque/force curves (Fig. 5c and d) throughout the same simulated frequencies. The figure also contains close-up views of the added-mass curves to show that the absolute variations are observed to be on the order of O(E-2) and O(E-1) for pitch and surge-pitch added mass, respectively. It is noted that the close-up views show only a portion of the frequency range but they are applicable to the entire x-axis. These absolute differences are important for the discussion in the following paragraph.

For motion about the center of mass (Fig. 6), the excitation force in surge, X_1 , torque in pitch, X_5 , and radiation damping (B_{55} , B_{15}) correlate very well between the two methods. While differences of up to 15% are present in the added mass solutions in both pitch and surge-pitch modes, the absolute variations are again observed to be on the order of O(E-2) and O(E-1) for pitch and surge-pitch added mass, respectively. The large percentage difference seen in this case, however, is magnified due to the smaller values (about 10 times smaller than the previous case) of

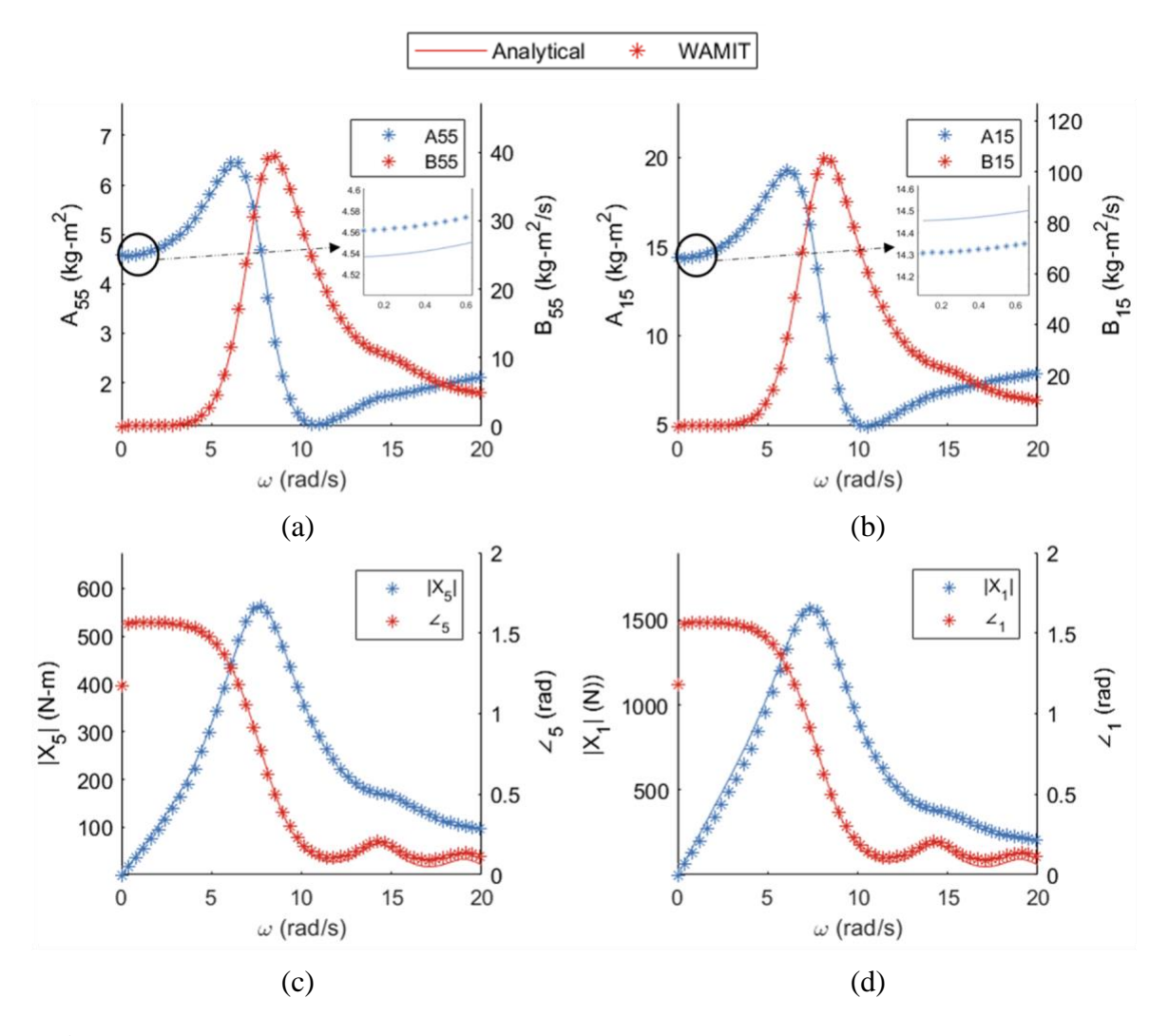


Figure 5 – Comparison of analytically derived (solid) and numerically derived (dashed) hydrodynamic coefficients. Outputs are computed with respect to the **hinge location**. (a) Pitch added mass (A_{55}) and radiation damping (B_{55}). (b) Surge-pitch added mass (A_{15}) and radiation damping (B_{15}). (c) Pitch excitation torque magnitude per wavelength ($|X_5|$) and phase (\angle_5). (d) Surge excitation force magnitude per wavelength ($|X_1|$) and phase (\angle_1).

the added mass coefficients. This could indicate that there is an inherent static variation between the two methods rather than a variation caused by the performance of the analytical model. Other reasons that could lead to the differences might be attributed to the flat plate assumption and the handling of the boundary element method for thin structures. Due to the thin plate nature, it is challenging to generate a good mesh for the simulation such that the panels on the thin side and the panels near the sides are comparable in dimension. In addition, modeling thin structures also leads to close proximity of the target and the source panels, which could result in numerical

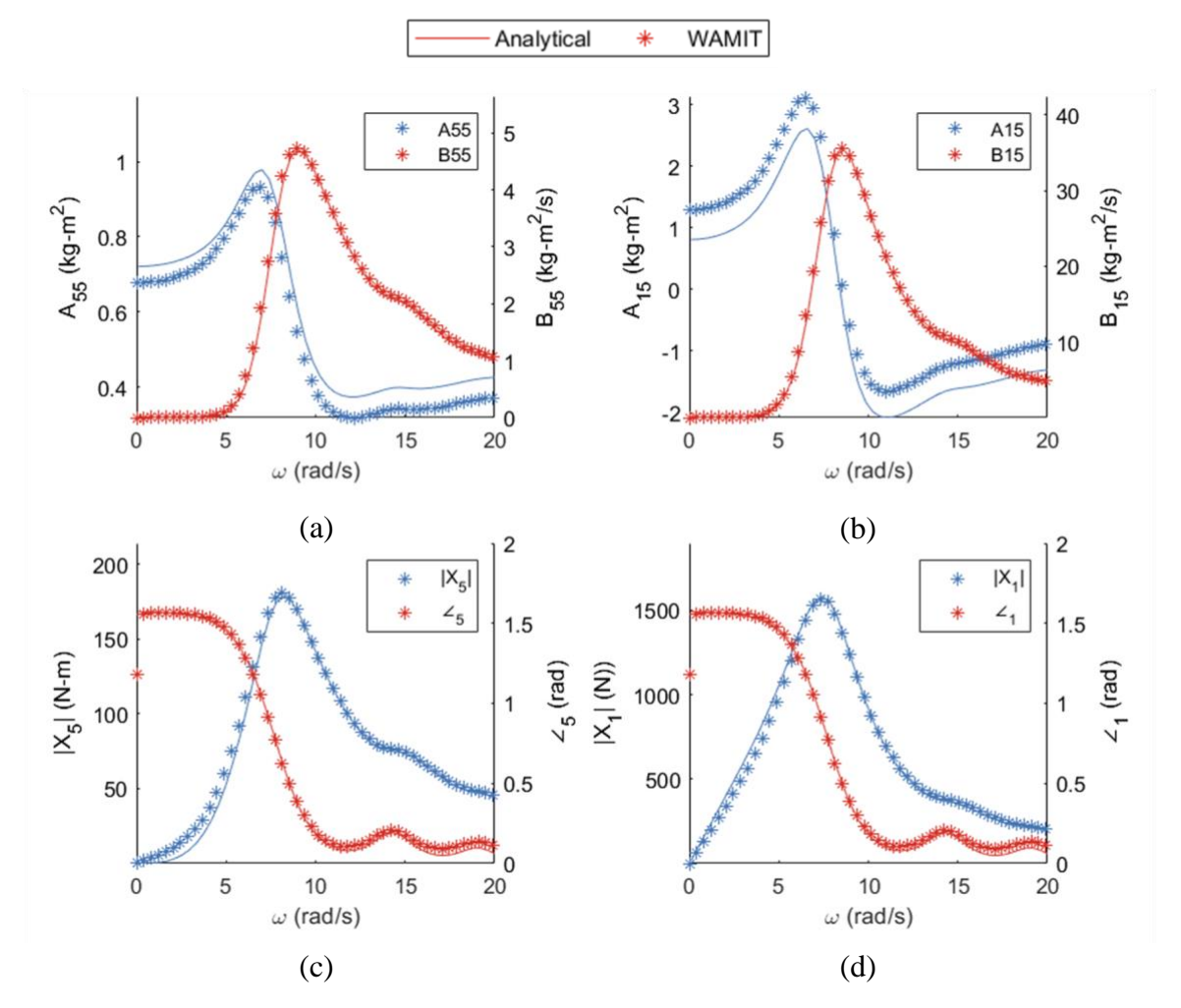


Figure 6 – Comparison of analytically derived (solid) and numerically derived (dashed) hydrodynamic coefficients. Outputs computed with respect to the **center of gravity**. (a) Pitch added mass (A_{55}) and radiation damping (B_{55}). (b) Surge-pitch added mass (A_{15}) and radiation damping (B_{15}). (c) Pitch excitation torque magnitude per wavelength ($|X_5|$) and phase (\angle_5). (d) Surge excitation force magnitude per wavelength ($|X_1|$) and phase (\angle_1).

modeling uncertainties (Sheng et al., 2022). It is noted that the current study has not carried out an extensive optimization of the mesh for WAMIT modeling. Future studies will be completed to explore these variations further.

Despite the slight differences, this section shows that the analytical model correlates very well with WAMIT numerical solutions. The strength of the analytical model becomes evident when the solution times are compared; whereas the WAMIT model used to produce validation results requires preparation on the order of hours and requires several minutes to run a single frequency step, the analytical model can be set up on the order of minutes and used to produce similar results, averaging less than one second to execute each frequency.

3.3. OSWEC Motion and Structural Loads – Comparison of Analytical, and WAMIT/WEC-Sim Approaches

This section compares the OSWEC response and foundation loads calculated by the proposed analytical formulas with those obtained from the numerical models (WAMIT/WEC-Sim). The wave conditions are the same as described previously. The results of pitch RAO and of the hinge forces and foundational torques are presented in Figs. 7 and 8, respectively. There is excellent agreement between the solutions of the two models over much of the frequency range. While it is not shown here, the phase was also relatively aligned. Slight variations are observed near the resonance frequency region for all parameters. This could be attributed to the challenge of estimating the hydrodynamic coefficients for thin structures, as discussed in the previous section. Further studies should be done to examine these effects. The dissimilarity in this case study, however, is small, and it could be neglected to simplify the analysis. In Fig. 8, the normalized magnitude of excitation wave loads/torques obtained in previous sections are also plotted for

comparison. The results show that the effect of wave load components are small (except at low periods) and the foundation reaction forces are mostly due to the flap's pitching motions.

The resonance frequency predicted by both models is approximately 1.9 s, which is close to the resonance frequency of the physical model at 1.76 s (Davis, 2021). The discrepancy is reasonable given the smaller thickness of the OSWEC used in this study, as well as the difference in foundation geometry. In this study, the foundation is represented by a 2D geometry with the same width and thickness as the OSWEC flap. In the experiments of (Davis, 2021), the foundation is modeled as a 3D circular cylinder.

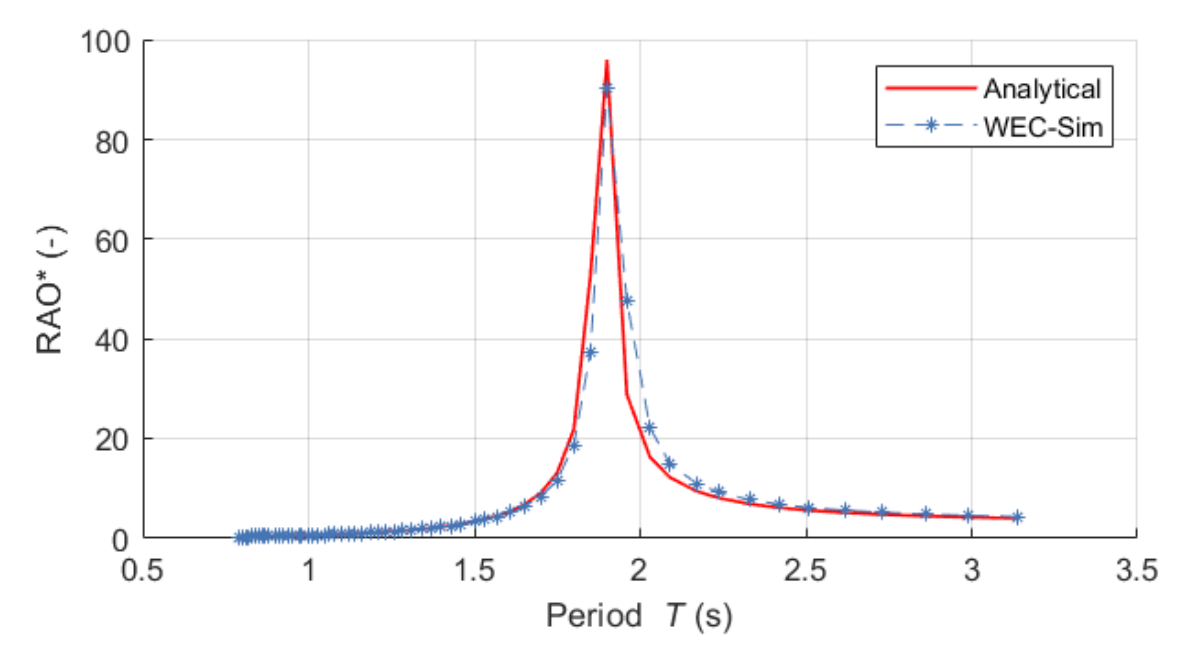


Figure 7 – Comparisons of analytical and WEC-Sim results for pitch RAO outputs.

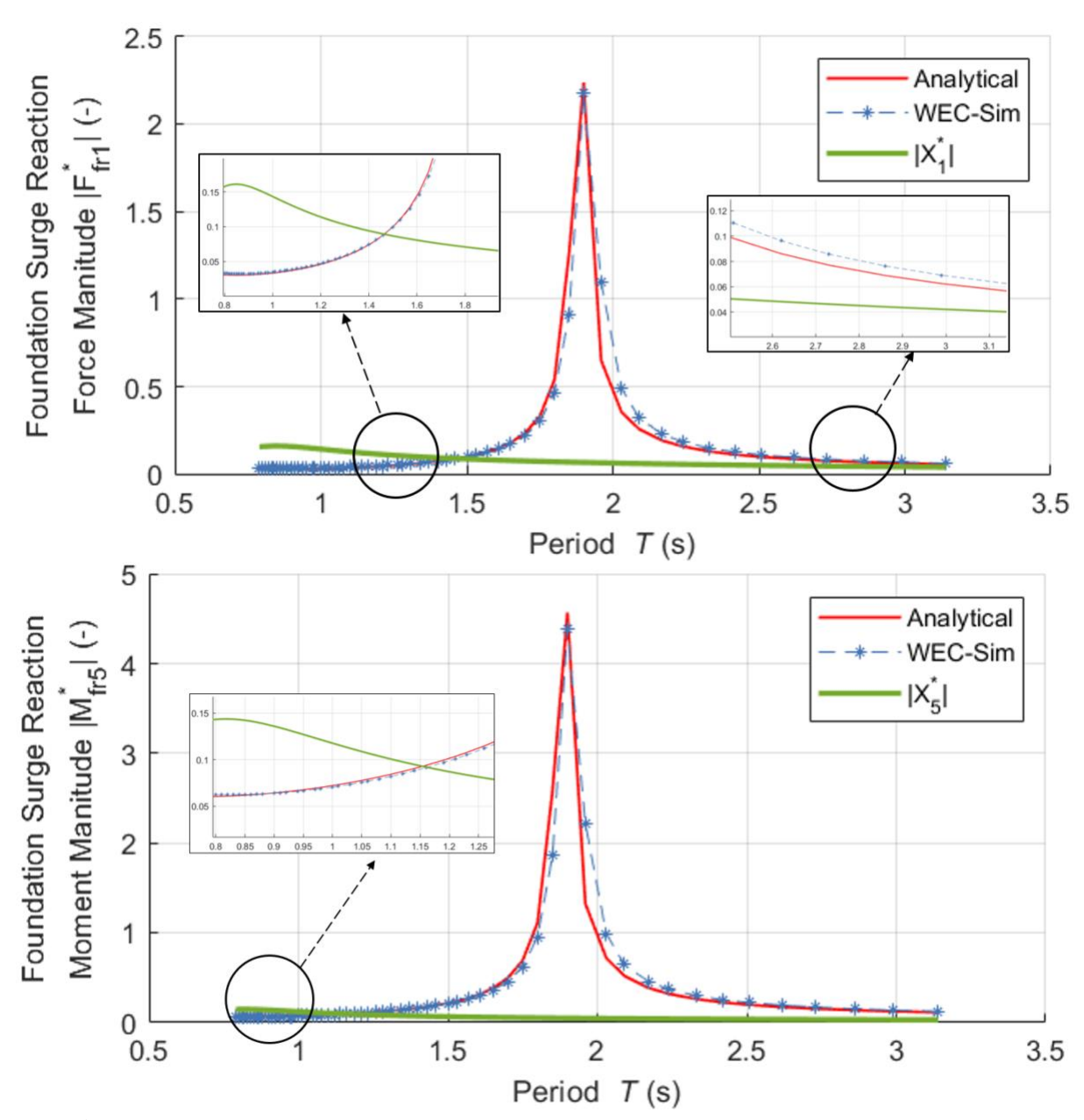


Figure 8 – Simulated foundation base reaction forces and moments. Wave excitation force/torque on the full system are also plotted for comparison. The results show that wave loads are small (except at low periods) and indicate that foundation reaction forces are mostly due to the flap's pitching motions. The components are nondimensionalized as $|F_{fr1}^*| = |F_{fr1}|/(\rho gh^2 a)$, $|M_{fr5}^*| = |M_{fr5}|/(\rho gh^2 aw)$, $|X^*| = |X|/(\rho gh^2)$.

4. Parametric Study and Discussion

4.1. Thickness Sensitivity Study

This section investigates the sensitivity of plate thickness on the analytical hydrodynamic solutions. The results shed light on the advantages and limitations of the proposed analytical formulas. Several WAMIT models with thickness-to-width ratio (p/w) ranging from 1:80, 1:40, 1:20, and 1:10 relative to the scale of the physical model are constructed and simulated over the same frequency range. Figs. 9a and 9b show sample comparisons of hydrodynamic coefficients from the analytical model and WAMIT with varying plate thicknesses. As the plate thickness gets larger, the results from the two approaches start to deviate. While the differences in the predicted added mass values occur mostly in the low- and high-frequency ranges, the variations of radiation damping coefficients are present around the curve peaks (5–10 rad/s). Outside this region, the

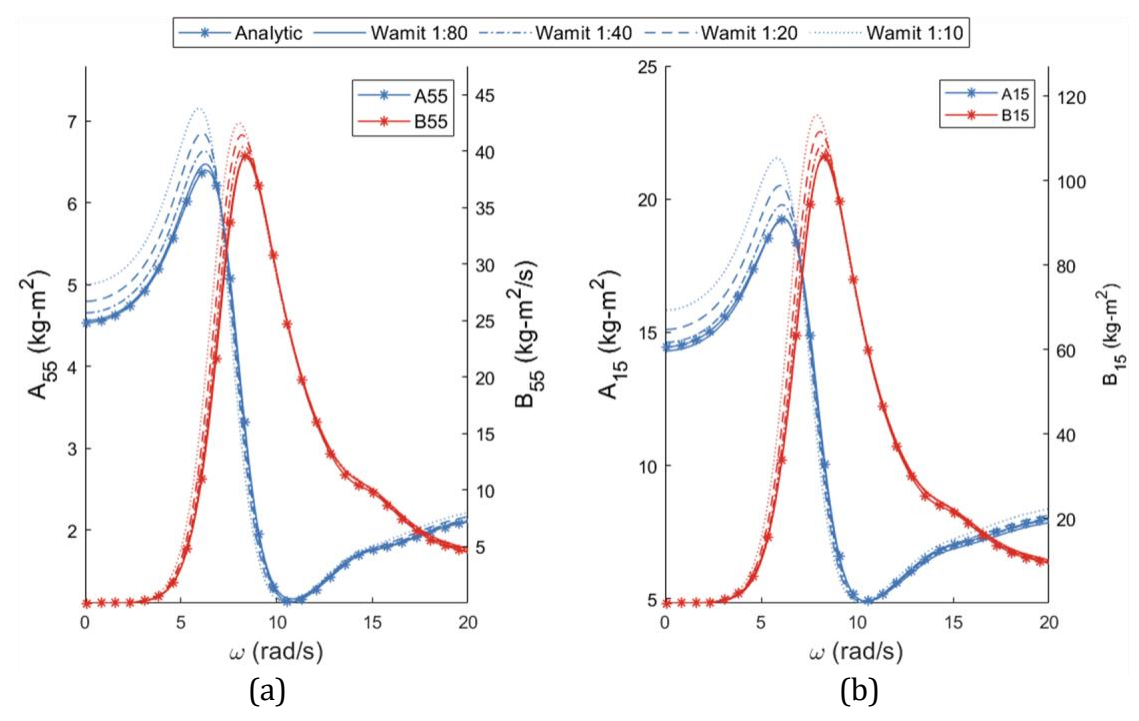


Figure 9 – Sample comparison of hydrodynamic coefficients from the analytical model and WAMIT with varying plate thicknesses. (a) Pitch added mass. (b) Surge-pitch added mass. As the plate gets thicker, the solutions between the two models start to deviate, with the WAMIT outputs growing larger. The peaks of these curves also shift to lower frequencies.

variations in radiation damping are small. The results also show a consistent shift to a lower-frequency region as the plate thickness increases. In order to compare these deviations more quantitatively, normalized errors, $\bar{\varepsilon}$, are calculated following Equation (69), for both cases (rotational motions with respect to the center of gravity and to the hinge):

$$\bar{\varepsilon} = \frac{S_{\text{Wamit}} - S_{\text{analytical}}}{\text{max}|S_{\text{Wamit}}|} * 100$$
 (69)

where *S* is the hydrodynamic parameter of interest.

From Figs. 10 and 11, except for the surge-pitch added mass values discussed previously, the analytical model and WAMIT compare very well, with maximum differences ranging from 3% for the thinnest plate (p/w = 1:80) to 10% for (p/w = 1:20), and 20% for the thickest plate (p/w = 1:10). The large variations come mostly from the hydrodynamic coefficient values. If only excitation forces/torques are considered, the differences between the two approaches are contained within 12% for all thicknesses studied. Given the significant reduction in computational times and model setup (a few minutes versus hours), this level of uncertainty is justifiable, especially during the initial phase of design parameter exploration. The analytical model is thus useful to narrow the design scope before a higher-fidelity model is employed.

4.2. Parametric Study of Power Production for a Range of Flap Heights and Widths

This section demonstrates the ability of analytical models to explore the design space of a WEC with computational ease (i.e., performing a sweep over a range of dimensions). A full-scale irregular wave state from the U.S. Department of Energy Wave Energy Prize (Driscoll et al., 2018) is used to define the environmental wave conditions of the demonstration. Full-scale irregular wave state 2 (IWS 2) was elected for use. The irregular sea state was defined by a Bretschneider wave energy spectrum (Equation (30)). The environmental conditions used in the demonstration are summarized in Table 3.

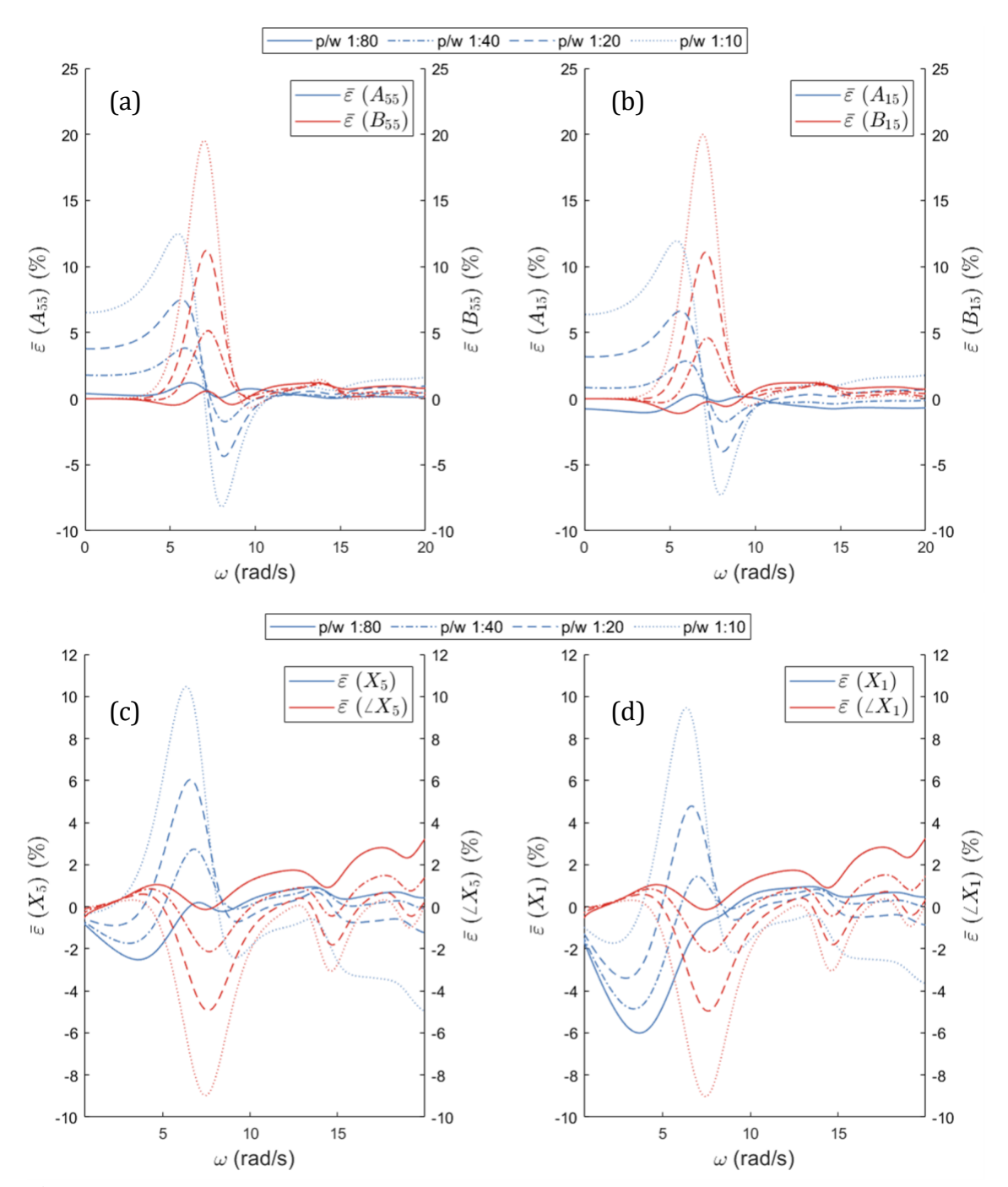


Figure 10 – Error quantifications of analytical model and WAMIT solutions for different plate thicknesses. (a) Pitch added mass. (b) Surge-pitch added mass. (c) Pitch excitation torque. (d) Surge excitation force. Outputs are computed with respect to the **hinge location**. The ratio of plate thickness to plate width $\left(\frac{p}{w}\right)$ ranges from 1:10 to 1:80.

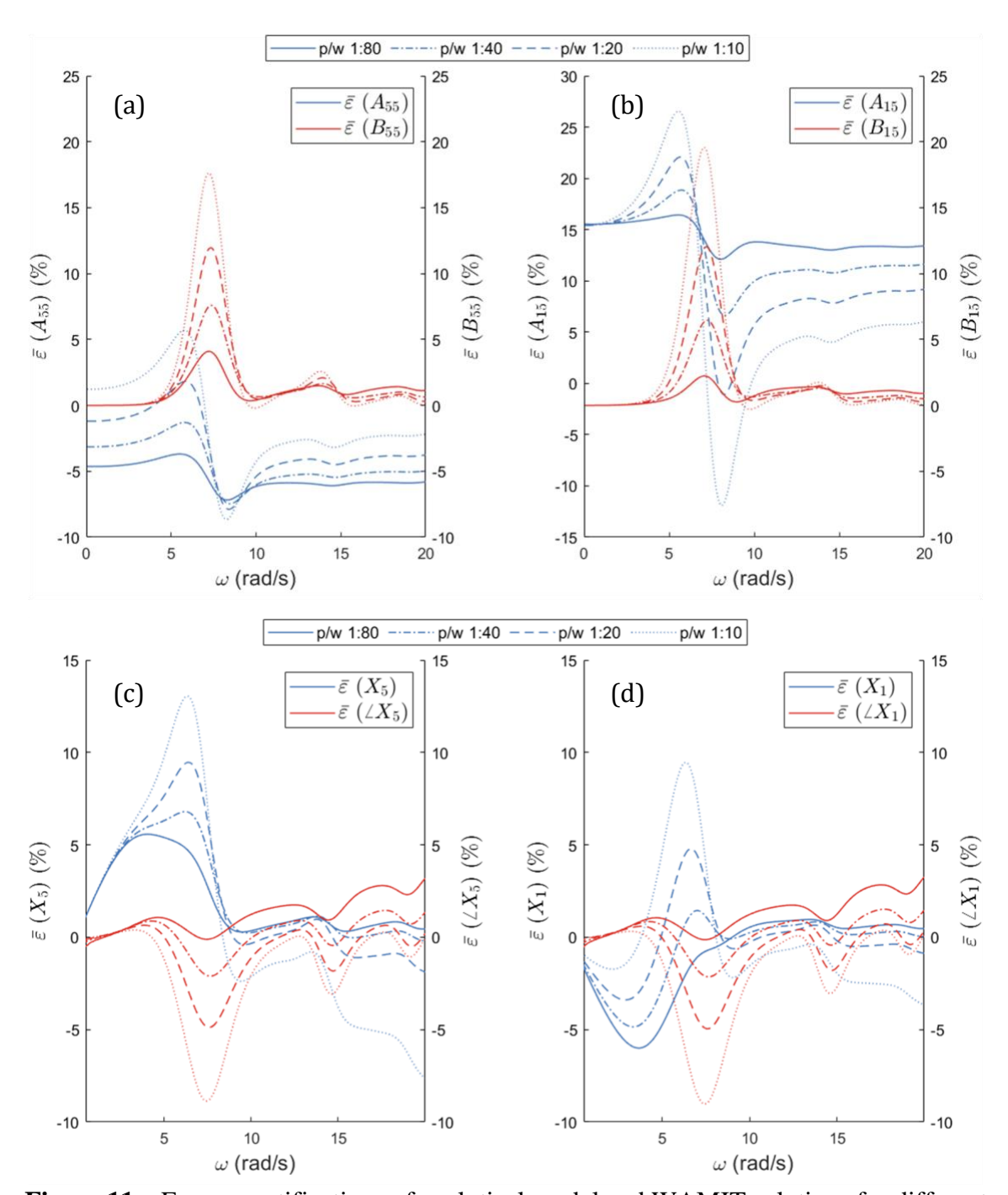


Figure 11 – Error quantifications of analytical model and WAMIT solutions for different plate thicknesses. (a) Pitch added mass. (b) Surge-pitch added mass. (c) Pitch excitation torque. (d) Surge excitation force. Outputs are computed with respect to the **center of gravity**. The ratio of plate thickness to plate width $\left(\frac{p}{w}\right)$ ranges from 1:10 to 1:80.

Table 3 - Environmental conditions used in the demonstration

Symbol	Name	Value	Unit
$S(\omega)$	Energy spectrum	Bretschneider	-
T_p	Peak period	9.86	S
H_s	Sig. wave height	2.64	m
ω_{min}	Min. frequency	0.25	rad s ⁻¹
ω_{max}	Max. frequency	3.00	rad s ⁻¹
$d\omega$	Frequency increment	0.01	rad s ⁻¹

Five dimensions define the bottom-raised OSWEC system: water depth h, flap height H_o , distance from the hinge to the seabed c, width w, and thickness p. If the height of the flap is constrained such that the flap always extends from the hinge to the free surface (i.e., $H_o = h - c$), the thickness is parameterized as a function of width (w/p = constant). If the mean water depth is assumed constant, the number of free dimensions can be reduced to two: the flap width and the distance from the hinge to the seabed.

Here, the flap width w ranges from 1/3 of the water depth to the full water depth (the flap is as wide as the water is deep) in increments of 1 m. The distance from the hinge to the seabed c ranges from 0 m to 2/3 of the water depth in increments of 1 m. Though the theoretical model is reliant on a thin plate assumption, a thickness is defined to obtain reasonable mass moment of inertia and body volume properties. The width-to-thickness ratio is held constant at w/p = 30. To parameterize mass, a mass density ρ_m equivalent to half the water density is assigned. For each set of dimensions, the body mass-moment of inertia and linear, combined hydrostatic and gravitational restoring coefficient are calculated using Equations (68) and (12), respectively. These dimensions and properties are defined in Table 4.

Variations in frequency-dependent pitch added mass, pitch radiation damping, and pitch excitation moment with normalized width (w/H_o) are presented in Fig. 12. Results are shown for a single flap height of $H_o = h/2$. As width is increased, these coefficients increase in magnitude,

and peak values shift toward lower frequencies. These trends are consistent with WAMIT results from Kurniawan and Moan (2012), who conducted a similar frequency-domain sweep across widths on a bottom-raised OSWEC. Similar trends have been well-documented in studies on bottom-fixed OSWECs (Gomes et al., 2015).

Table 4 - Dimensions and properties of demonstration model					
Symbol	Name	Value	Unit		
h	Water depth	30	m		
c	Hinge to seabed	0:1:20:a	m		
H_o	Flap height	10:1:30	m		
W	Flap width	10-30	m		
w/p	Flap width-to-thickness ratio	30	m/m		
$ ho_m$	Mass density	500	kg m ⁻³		

a start:stepsize:stop

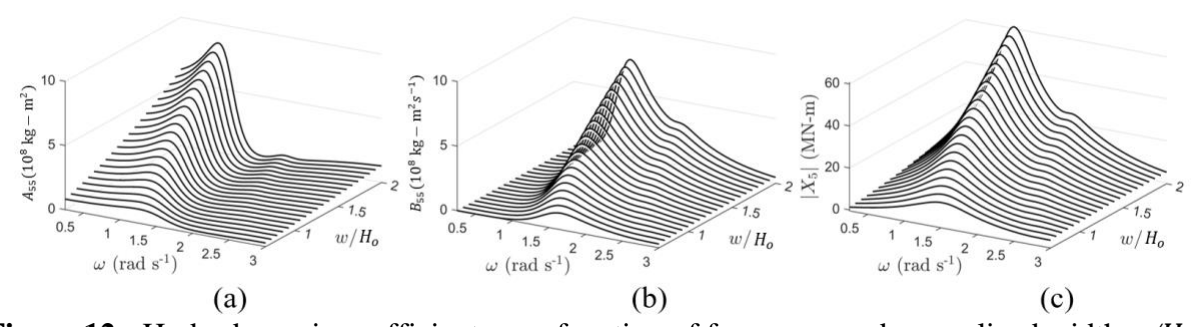


Figure 12 - Hydrodynamic coefficients as a function of frequency and normalized width w/H_o for a constant flap height $H_o = h/2$: (a) pitch added mass; (b) pitch radiation damping; (c) excitation pitch moment.

Performance characteristics, displayed as a function of the normalized distance to seabed (c/h) and normalized width (w/h), are presented in Fig. 13. It is noted that color bars are not included in all Fig. 13 plots to reduce visual clutter. The colors, however, are scaled with their respective z-axis values. The capture width ratio (Fig. 13a) is representative of the ratio of power absorbed by an ideal PTO during operation in the IWS 2 sea state to the total wave power available in that sea state following Equations (28) and (31). The surge force at the hinge (Fig. 13b) and its resulting

contribution to the bending moment about the foundation base (Fig. 13c) are taken as the maximum values in response to a regular design wave at the significant wave height and peak period.

Under the constraints used in the demonstration calculations, the capture width ratio increases dramatically with increasing width and decreases slightly as the distance from the seabed increases. The maximum surge hinge reaction force follows a similar trend. This result is expected: As the OSWEC grows in width or height, its face occupies a larger portion of the water cross section, hence increasing the magnitude of the hydrodynamic coefficients and excitation loads. The foundation base bending moment is maximized at the full width and at the largest distance from the seabed. Though the surge hinge reaction force decreases with increasing distance, this change is overcome by the increase in moment arm as the hinge is moved further from the seabed. Additional constraints unique to each study could be imposed to further narrow the optimal dimensions. These constraints could include knowledge of the structural limits of the internal hinge support mechanisms (e.g., bearings, shafts, shaft mounts), as well as the geometry and material limits of the foundation. The trade-off between power absorption and loading on OSWEC designs has been the subject of previous studies (e.g., Tom et al., 2017).

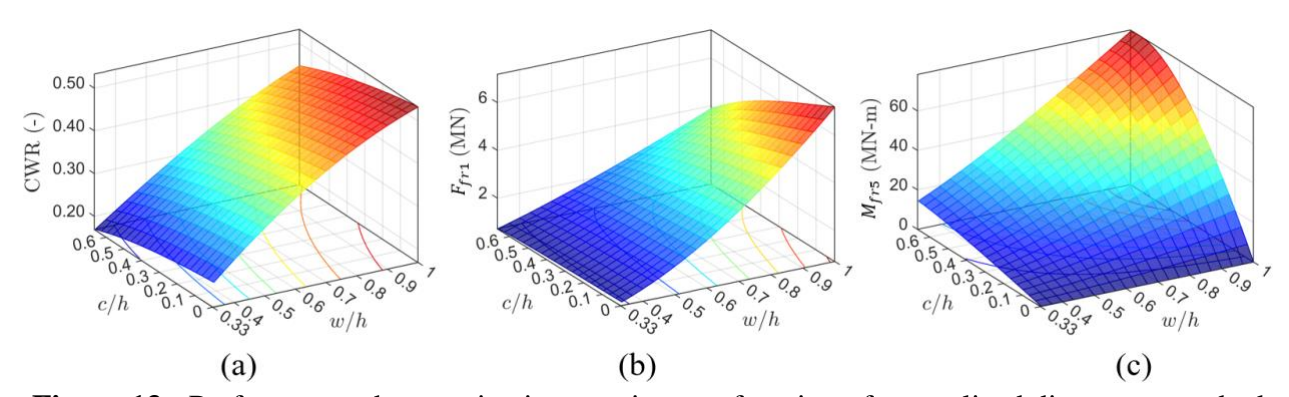


Figure 13 - Performance characterization metrics as a function of normalized distance to seabed *c/h* and normalized width *w/h*: (a) capture width ratio; (b) surge hinge reaction force; (c) foundation base bending moment. Colors correspond to the z-axis values.

5. Conclusion

The current study presents theoretical formulations to evaluate the fundamental parameters of a bottom-raised OSWEC device, including foundation loads, the RAO, hydrodynamic coefficients, and excitation forces/torques. Specifically, the study develops closed-form equations for pitch-pitch and surge-pitch added inertia and radiation damping for the OSWEC body pitching at the hinge and at the center of gravity. These parameters are then utilized to investigate capture width ratio (power production) and the structural load on the support foundations resulting from the motion of the OSWEC.

The proposed analytical model is benchmarked against numerical simulations using WAMIT and WEC-Sim. The comparisons demonstrate excellent agreement between the two approaches for the aforementioned parameters. Although variations are observed in the added mass solutions for pitch-pitch and surge-pitch modes, the overall correlation between the models is strong. The differences in pitch-pitch and surge-pitch added mass are about 15% while variations in other parameters of interest are less than 2%. The analytical model demonstrates the advantage of significantly reduced computational time and setup complexity compared to the numerical models.

To determine the validity of the flat plate assumption (which is inherent to the analytical solution), this study also examines the sensitivity of plate thickness on the analytical hydrodynamic solutions. A range of plate thickness was tested with thickness-to-width ratios ranging from 1:80 to 1:10. The results show that as the thickness increases, the deviations of hydrodynamic coefficients with numerical solutions also grow from 3% to 25% correspondingly. For excitation forces and torques, however, the differences are contained within 12%. This level of uncertainty is reasonable, especially during the initial design phase, where the analytical model can be utilized to explore the design space before employing higher-fidelity models.

Furthermore, the study demonstrates the use of theoretical models in the design of OSWEC devices, allowing for easy exploration of the design space. By varying dimensions such as flap width and distance from the hinge to the seabed, the study examines the performance characteristics of the OSWEC, including capture width ratio, surge force at the hinge, and bending moment about the foundation base. The results show that increasing the width of the OSWEC leads to higher capture width ratio and surge hinge reaction force, while the foundation base bending moment is maximized at the full width and the largest distance from the seabed.

Overall, the proposed analytical model provides a valuable tool for evaluating the performance and loads of bottom-raised OSWEC devices. Its accuracy and computational efficiency make it suitable for initial design exploration and parameter optimization, complementing more time-consuming numerical models such as WAMIT and WEC-Sim. Further studies can be conducted to improve the analytical model's accuracy, especially considering the limitations of the thin plate assumption.

Acknowledgements

This article has been authored by an employee of National Technology & Engineering Solutions of Sandia, LLC under Contract No. DE-NA0003525 with the U.S. Department of Energy (DOE). The employee owns all right, title and interest in and to the article and is solely responsible for its contents. This work was authored in part by the National Renewable Energy Laboratory, operated by Alliance for Sustainable Energy, LLC, for the U.S. Department of Energy (DOE) under Contract No. DE-AC36-08GO28308. Funding provided by the U.S. Department of Energy Office of Energy Efficiency and Renewable Energy Water Power Technologies Office. The United States Government retains and the publisher, by accepting the article for publication, acknowledges that the United States Government retains a non-exclusive, paid-up, irrevocable, world-wide license to publish or reproduce the published form of this article or allow others to do so, for United States Government purposes. The DOE will provide public access to these results of federally sponsored research in accordance with the DOE Public Access Plan https://www.energy.gov/downloads/doe-public-access-plan.

This paper describes objective technical results and analysis. Any subjective views or opinions that might be expressed in the paper do not necessarily represent the views of the U.S. Department of Energy or the United States Government.

Appendix A

Retardation Function in Frequency Domain

Using the proposed model, the retardation function in the frequency domain can be derived from equation (64) based on factors such as radiation damping, frequency-dependent added mass, and added mass at infinite frequency. Table A1 and Fig. A1 present comparisons between the model outputs and those obtained from WAMIT. It is noted that the WAMIT results discussed in this section employed the thinnest flap geometry (with a thickness to width ratio of 1:80).

In comparing the added mass at infinite frequency, a strong correlation between the two models is observed, with differences typically within 3% for the case where the flap rotates around the hinge. On the other hand, for the scenario where the flap rotates around its center of mass, significant disparities between the models are noted. However, it is important to highlight that the added mass at infinite frequency tends towards zero in this configuration. The substantial differences observed are likely attributed to numerical errors rather than inherent physical variations between the models.

T	able A1 – Added ma	ss at infinite freq	quency comparison				
	K ₅₅	$ar{arepsilon}\left(\% ight)$	K ₁₅	$\bar{\varepsilon}\left(\% ight)$			
	Flap rota	ates around the h	inge	l			
Analytical model	2.6233	2.98	9.3102	0.01			
WAMIT	2.7040		9.3230	0.01			
Flap rotates around its center of mass							
Analytical model	0.5000	7.78	-0.328	60.0			
WAMIT	0.4639		-0.820	. 00.0			
$\bar{\varepsilon}$: variations (%) bet	ween the proposed m	nodel and WAM	IT.				

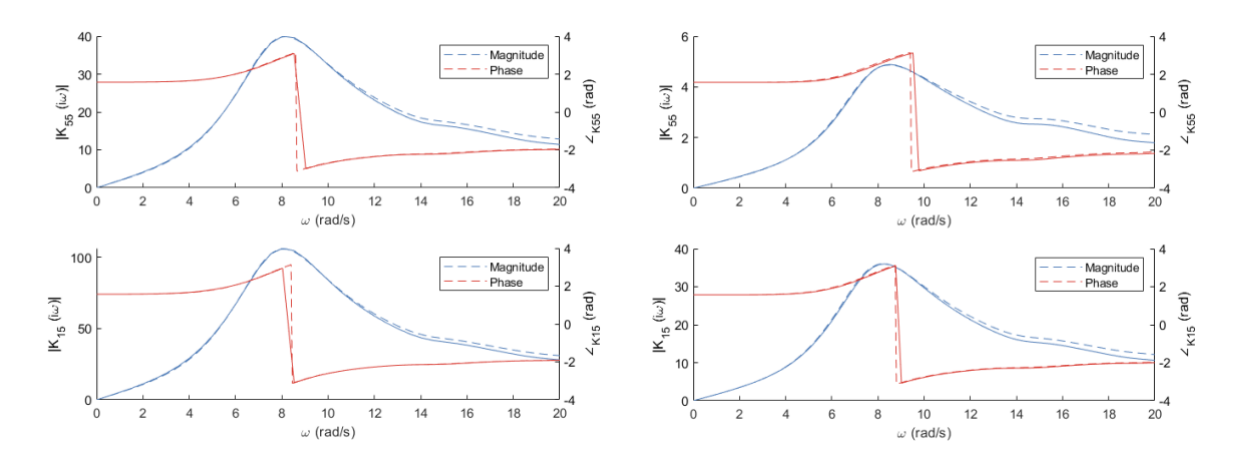


Figure A1 – The comparison of the retardation function, $K(i\omega)$, in the frequency domain is depicted for both magnitudes (blue curves) and phases (red curves). Strong correlations are observed between the results obtained from WAMIT and those derived from the proposed model. In the figures, solid lines represent the solutions obtained from the analytical model, while dashed lines denote the outputs from WAMIT. The left panel illustrates the results for the case where the flap rotates around the hinge, while the right panel presents solutions for the setup where the flap rotates around its center of mass.

Appendix B

Hydrodynamic Analytical Model Using Haskind-Hanaoka Approach

The analytical model can be validated by evaluating the excitation torque on the structure employing two approaches. The first method, which is described in Section 2, employs the surface integral of the scattered potential while the second technique utilizes the Haskind-Hanaoka relation. Using the Haskind-Hanaoka relation for a 3D floating body, the excitation torque is formulated as (see Chapter 8 in Mei et al. (2005) for derivation details):

$$X_{j} = -\frac{4}{k} \rho g \mathcal{A}_{j}^{R} \left(\frac{\pi}{2}\right) \cos \theta \tag{70}$$

where j denotes the body motion mode. \mathcal{A}^R is called the angular variation of the radially spreading wave (Mei et al., 2005) and has the unit of time. Moreover, the general form of asymptotic behavior of the radiation potential in the far field ($\xi \to \infty$) can be written as (Equation 8.6.12 in Mei et al. (2005)):

$$\sum_{n=0}^{\infty} \phi_{jn}^{R} \sim \frac{ig\mathcal{A}_{j}^{R}(\eta)}{\omega} \frac{\cosh k(h+z)}{\cosh kh} \sqrt{\frac{2}{\pi kr}} e^{i\left(kr - \frac{\pi}{4}\right)}$$
 (71)

where $r=\frac{we^{\xi}}{4}$ is the radius expressed in terms of the radial elliptic coordinate ξ . Equating the right-hand side with the expressions of ϕ_{jn}^R , and using the asymptotic formula of the Hankel-Mathieu function of the first kind, $Ho_{2m+1}^{(1)}(\xi \to \infty, \tau_n)$, as (Gutiérrez-Vega, 2000):

$$Ho_{2m+1}(\xi \to \infty, \tau_n) = -\frac{S_{2m+1}}{\sqrt{\tau_n}B_1} \sqrt{\frac{2}{\pi\sqrt{\tau_n}e^{\xi}}} e^{i\left(\sqrt{\tau_n}e^{\xi} - \frac{3\pi}{4}\right)}$$
(72)

with $\tau_n = \left(\frac{wk_n}{4}\right)^2$

$$Ho_{2m+1}(\xi \to \infty, \tau_n) = -\frac{4S_{2m+1}}{wk_n B_1} \sqrt{\frac{2}{\pi k_n r}} e^{i(k_n r - \frac{3\pi}{4})}$$
 (73)

where

$$S_{2m+1} = s e_{\eta_{2m+1}}(0, \tau_n) s e_{2m+1} \left(\frac{\pi}{2}, \tau_n\right)$$
 (74)

 se_{η} denotes the derivatives of se with respect to η . $\mathcal{A}_{j}^{R}(\eta)$ can then be found for surge and pitch excitation forces/torques as

$$\mathcal{A}_{1}^{R}(\eta) = -\sum_{m=0}^{\infty} \frac{2\omega Z_{o} \lambda_{o} \left[se_{2m+1} \left(\frac{\pi}{2}, \tau_{n} \right) \right]^{2} se_{\eta_{2n+1}}(0, \tau_{n})}{gk_{o} Ho_{\xi_{2m+1}}(0, \tau_{n})}$$
(75)

and

$$\mathcal{A}_{5}^{R}(\eta) = -\sum_{m=0}^{\infty} \frac{2\omega Z_{o} f_{o} \left[s e_{2m+1} \left(\frac{\pi}{2}, \tau_{n} \right) \right]^{2} s e_{\eta_{2n+1}}(0, \tau_{n})}{g k_{o} H o_{\xi_{2m+1}}(0, \tau_{n})}$$
(76)

 λ_o and f_o are presented in Equations (51) and (63). Substituting these into Equation (70), X_1 and X_5 can be calculated. Comparisons of solutions from the two approaches are presented in Fig. B1. Employing m=7 (the number of orders used in evaluating the Mathieu functions), the differences between the two approaches are estimated to be in the order of O(E-12).

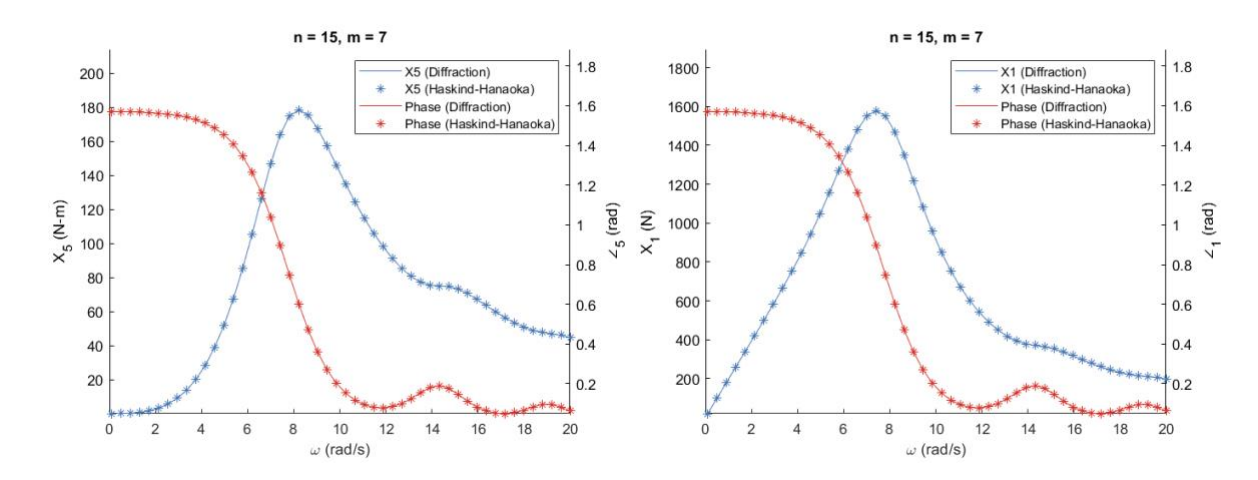


Figure B1 – Comparison of wave excitation pitch and surge moment magnitudes and phases using 1) Diffraction method and 2) Haskind-Hanaoka relation. Left: pitch excitation torque, X_5 . Right: surge excitation force, X_1 . The converged results were obtained with n = 15, m = 7 to achieve an order of O(E-12) differences between the two solutions.

References

- 1. Ancellin, M. and Dias, F., 2019. Capytaine: A Python-based linear potential flow solver. *Journal of Open Source Software*, *4*(36), p.1341.
- 2. Ancellin, M., 2022. Github Capytaine: a linear potential flow BEM solver with Python. https://https://github.com/capytaine/capytaine
- 3. Cameron, L., Doherty, R., Henry, A., Doherty, K., Van't Hoff, J., Kaye, D., Naylor, D., Bourdier, S. and Whittaker, T., 2010, October. Design of the next generation of the Oyster wave energy converter. In *3rd international conference on ocean energy* (Vol. 6, p. 1e12). ICOE Bilbao, Spain.
- 4. Chakrabarti, S.K., 1994. Offshore structure modeling (Vol. 9). world scientific.
- 5. Chatjigeorgiou, I.K. and Katsardi, V., 2018. Hydrodynamics and near trapping effects in arrays of multiple elliptical cylinders in waves. *Ocean Engineering*, *157*, pp.121-139.
- 6. Choiniere, M., Davis, J., Nguyen, N., Tom, N., Fowler, M. and Thiagarajan, K., 2022. Hydrodynamics and load shedding behavior of a variable-geometry oscillating surge wave energy converter (OSWEC). *Renewable Energy*.
- 7. Choiniere, M.A., Tom, N.M. and Thiagarajan, K.P., 2019. Load shedding characteristics of an oscillating surge wave energy converter with variable geometry. *Ocean Engineering*, 186, p.105982.
- 8. Clemente, D., Rosa-Santos, P. and Taveira-Pinto, F., 2021. On the potential synergies and applications of wave energy converters: A review. *Renewable and Sustainable Energy Reviews*, 135, p.110162.
- 9. Coe, R.G., Bacelli, G., Spencer, S.J., Forbush, D. and Dullea, K., 2019. *Advanced WEC dynamics and controls MASK3 test* (No. SAND-2019-15428). Sandia National Laboratories (SNL), Albuquerque, NM, and Livermore, CA (United States).
- 10. Cole Burge. Personal Communications. 2020.
- 11. Davis, J.R., 2021. Design and Testing of a Foundation Raised Oscillating Surge Wave Energy Converter.
- 12. Dean, R.G. and Dalrymple, R.A., 1991. Water wave mechanics for engineers and scientists (Vol. 2). world scientific publishing company.
- 13. Drew, B., Plummer, A.R. and Sahinkaya, M.N., 2009. A review of wave energy converter technology.
- 14. Driscoll, F.R., Weber, J.W., Jenne, D.S., Thresher, R.W., Fingersh, L.J., Bull, D., Dallman, A., Gunawan, B., Ruehl, K., Newborn, D. and Quintero, M., 2018. *Methodology to calculate the ACE and HPQ metrics used in the Wave Energy*

- *Prize* (No. NREL/TP-5000-70592). National Renewable Energy Lab.(NREL), Golden, CO (United States).
- 15. Folley, M. and Whittaker, T.J.T., 2009. Analysis of the nearshore wave energy resource. *Renewable energy*, *34*(7), pp.1709-1715.
- 16. Foteinis, S. and Tsoutsos, T., 2017. Strategies to improve sustainability and offset the initial high capital expenditure of wave energy converters (WECs). *Renewable and Sustainable Energy Reviews*, 70, pp.775-785.
- 17. Garavelli, L., Freeman, M.C., Tugade, L.G., Greene, D. and McNally, J., 2022. A feasibility assessment for co-locating and powering offshore aquaculture with wave energy in the United States. *Ocean & Coastal Management*, 225, p.106242.
- 18. Gomes, R.P.F., Lopes, M.F.P., Henriques, J.C.C., Gato, L.M.C. and Falcão, A.F.O., 2015. The dynamics and power extraction of bottom-hinged plate wave energy converters in regular and irregular waves. *Ocean Engineering*, *96*, pp.86-99.
- 19. Gomes, R.P.F., Lopes, M.F.P., Henriques, J.C.C., Gato, L.M.C. and Falcão, A.F.O., 2015. The dynamics and power extraction of bottom-hinged plate wave energy converters in regular and irregular waves. *Ocean Engineering*, *96*, pp.86-99.
- 20. GutiÈrrez-Vega, J.C., 2000. ìFormal analysis of the propagation of invariant optical Öelds in elliptic coordinates. Ph. D. Thesis, INAOE, MÈxico.
- 21. Gutiérrez-Vega, J.C., Rodriguez-Dagnino, R.M., Meneses-Nava, M.A. and Chávez-Cerda, S., 2003. Mathieu functions, a visual approach. *American Journal of Physics*, 71(3), pp.233-242.
- 22. Howard, D., Whittaker, T. and Doherty, K., 2009. Foundation load analysis of oyster using a five degree of freedom load transducer. In *Proceedings of the 8th European Wave & Tidal Energy Conference, Uppsala, Sweden*.
- 23. Inman, D.J., 2008. Engineering vibration. Upper Saddle.
- 24. Jenne, D.S., Yu, Y.H. and Neary, V., 2015. *Levelized cost of energy analysis of marine and hydrokinetic reference models* (No. NREL/CP-5000-64013). National Renewable Energy Lab.(NREL), Golden, CO (United States).
- 25. Kasanen, E., 2015, November. AW-Energy—Positive experiences of the Waveroller in Portugal and France. In *Proceedings of the WavEC Annual Seminar and International B2B Meetings, Lisbon, Portugal* (pp. 15-17).
- 26. Kelly, M., Tom, N., Yu, Y.H., Thresher, R. and Abbas, N., 2017, June. Development of the second-generation oscillating surge wave energy converter with variable geometry. In *The 27th International Ocean and Polar Engineering Conference*. OnePetro.

- 27. Kurniawan, A. and Moan, T., 2012. Characteristics of a pitching wave absorber with rotatable flap. *Energy Procedia*, 20, pp.134-147.
- 28. Malali, P. and Marchand, K., 2020. Assessment of currently available ocean wave energy conversion systems using technology readiness levels. *International Journal of Renewable Energy Technology*, 11(2), pp.126-146.
- 29. McCormick, M.E., 2007. Ocean Wave Energy Conversion Dover Publication Inc. *Chapter 4*.
- 30. McCormick, M.E., 2007. Ocean Wave Energy Conversion. Dover Publication.
- 31. Mei, C.C., Stiassnie, M.A. and Yue, D.K.P., 2005. *Theory and applications of ocean surface waves:* Part 2: Nonlinear Aspects, World Scientific, 2005
- 32. Michele, S., Sammarco, P. and d'Errico, M., 2016. Theory of the synchronous motion of an array of floating flap gates oscillating wave surge converter. *Proceedings of the Royal Society A: Mathematical, Physical and Engineering Sciences*, 472(2192), p.20160174.
- 33. Michele, S., Sammarco, P., d'Errico, M., Renzi, E., Abdolali, A., Bellotti, G. and Dias, F., 2015. Flap gate farm: From Venice lagoon defense to resonating wave energy production. Part 2: Synchronous response to incident waves in open sea. *Applied Ocean Research*, *52*, pp.43-61.
- 34. Nguyen, N., Davis, J., Thiagarajan, K., Tom, N. and Burge, C., 2021. *Optimizing Power Generation of a Bottom-Raised Oscillating Surge Wave Energy Converter Using a Theoretical Model* (No. NREL/CP-5700-79929). National Renewable Energy Lab.(NREL), Golden, CO (United States).
- 35. Noad, I. and Porter, R., 2015. Wave energy absorption by submerged flap-type oscillating wave surge converters. In *Proceedings of the 11th European wave and tidal energy conference, Nantes*.
- 36. Ochs, M.E. and Bull, D.L., 2013. *Technological Cost-Reduction Pathways for Oscillating Water Column Wave Energy Converters in the Marine Hydrokinetic Environment* (No. SAND2013-7205). Sandia National Lab.(SNL-NM), Albuquerque, NM (United States).
- 37. PB3 PowerBuoy, 2020. *Ocean Power Technologies*. Available from https://oceanpowertechnologies.com/news/pb3-powerbuoy-celebrates-one-year-of-maintenance-free-continuous-operation-in-the-adriatic-sea/ (access date 6 August 2022).
- 38. Renzi, E. and Dias, F., 2012. Resonant behaviour of an oscillating wave energy converter in a channel. *Journal of Fluid Mechanics*, 701, pp.482-510.
- 39. Renzi, E. and Dias, F., 2013. Hydrodynamics of the oscillating wave surge converter in the open ocean. *European Journal of Mechanics-B/Fluids*, 41, pp.1-10.
- 40. Renzi, E. and Dias, F., 2013. Relations for a periodic array of flap-type wave energy converters. *Applied Ocean Research*, *39*, pp.31-39.

- 41. Ross, D., 1995. Power from the Waves. Oxford University Press, USA.
- 42. Schmitt, P. and Elsaesser, B., 2015. On the use of OpenFOAM to model oscillating wave surge converters. *Ocean Engineering*, *108*, pp.98-104.
- 43. Sheng, W., Tapoglou, E., Ma, X., Taylor, C.J., Dorrell, R.M., Parsons, D.R. and Aggidis, G., 2022. Hydrodynamic studies of floating structures: Comparison of wave-structure interaction modelling. *Ocean Engineering*, 249, p.110878.
- 44. Shoring Up Wave Energy's Bottom Line Through Variable-Geometry WEC Designs. National Renewable Energy Laboratory, 2021. Available from https://www.nrel.gov/news/program/2021/shoring-up-wave-energys-bottom-line-through-variable-geometry-wec-designs.html (access date 6 August 2022)
- 45. Techet, A.H., 2005. 13.42 Design Principles for Ocean Vehicles.
- 46. Tom, N.M., Yu, Y.H. and Wright, A.D., 2017. *Balancing the Power-to-Load Ratio for a Novel Variable Geometry Wave Energy Converter with Nonideal Power Take-Off in Regular Waves* (No. NREL/CP-5000-68082). National Renewable Energy Lab.(NREL), Golden, CO (United States).
- 47. Trueworthy, A. and DuPont, B., 2020. The wave energy converter design process: Methods applied in industry and shortcomings of current practices. *Journal of Marine Science and Engineering*, 8(11), p.932.
- 48. van Rij, J., Yu, Y.H., Guo, Y. and Coe, R.G., 2019. A wave energy converter design load case study. *Journal of Marine Science and Engineering*, 7(8), p.250.
- 49. WAMIT theory manual at https://www.wamit.com/Publications/tmanual.pdf.
- 50. Weisstein, E.W., 2003. Elliptic cylindrical coordinates. https://mathworld. wolfram.
- 51. Whittaker, T. and Folley, M., 2012. Nearshore oscillating wave surge converters and the development of Oyster. *Philosophical Transactions of the Royal Society A: Mathematical, Physical and Engineering Sciences*, 370(1959), pp.345-364.
- 52. Yu, Y.H., Li, Y., Hallett, K. and Hotimsky, C., 2014, June. Design and analysis for a floating oscillating surge wave energy converter. In *International Conference on Offshore Mechanics and Arctic Engineering* (Vol. 45547, p. V09BT09A048). American Society of Mechanical Engineers.
- 53. Yu, Y.-H., Ruehl, K., Van Rij, J., Tom, N., Forbush, D., Ogden, D., Keester, A., Leon, J. 2020. WEC-Sim (Version v4.2), DOI 10.5281/zenodo.3924764.463
- 54. Zheng, S. and Zhang, Y., 2016. Wave radiation from a truncated cylinder in front of a vertical wall. *Ocean Engineering*, 111, pp.602-614.